

Determining Central Black Hole Masses in Distant Active Galaxies and Quasars. II. Improved Optical and UV Scaling Relationships.¹

Marianne Vestergaard² and Bradley M. Peterson³

ABSTRACT

We present four improved empirical relationships useful for estimating the central black hole mass in nearby AGNs and distant luminous quasars alike using either optical or UV single-epoch spectroscopy. These mass-scaling relationships between line widths and luminosity are based on recently improved empirical relationships between the broad-line region size and luminosities in various energy bands and are calibrated to the improved mass measurements of nearby AGNs based on emission-line reverberation mapping. The mass-scaling relationship based on the $H\beta$ line luminosity allows mass estimates for low-redshift sources with strong contamination of the optical continuum luminosity by stellar or non-thermal emission, while that based on the $C\text{IV } \lambda 1549$ line dispersion allows mass estimates in cases where only the line dispersion (as opposed to the FWHM) can be reliably determined. We estimate that the absolute uncertainties in masses given by these mass-scaling relationships are typically around a factor of 4. We include in an Appendix mass estimates for all the Bright Quasar Survey (PG) quasars for which direct reverberation-based mass measurements are not available.

Subject headings: galaxies: active — galaxies: fundamental parameters — galaxies: high-redshift — galaxies: Seyfert — quasars: emission lines — ultraviolet: galaxies

1. Introduction

A problem of current interest is determination of the mass function of the central black holes in active galactic nuclei (AGNs) and quasars over the history of the Universe in order to determine how these black holes evolve with time. Unfortunately, measurement of black hole masses by direct methods such as modeling of stellar or gas dynamics requires high spatial resolution and is thus

¹ Based in part on observations made with the NASA/ESA Hubble Space Telescope, obtained from the Data Archive at the Space Telescope Science Institute, which is operated by the Association of Universities for Research in Astronomy, Inc., under NASA contract NAS 5-26555.

²Steward Observatory, University of Arizona, 933 N. Cherry Avenue, Tucson, AZ 85718. Email: mvester-gaard@as.arizona.edu

³Department of Astronomy, The Ohio State University, 140 West 18th Avenue, Columbus, OH 43210-1773. Email: peterson@astronomy.ohio-state.edu

limited to relatively nearby galaxies. Moreover, the brightness of the AGN itself makes it extremely difficult to observe suitable stellar absorption lines for dynamical studies within the black hole radius of influence, and the complex gas dynamics in AGNs frustrate attempts to disentangle the emission-line kinematics. Megamaser dynamics have been used successfully to measure the black hole mass in NGC 4258 (Miyoshi et al. 1995), but this required particular fortunate circumstances that do not seem to be generally realized. Thus, for AGNs and quasars, the most promising method for measuring black hole masses is reverberation mapping of the broad emission lines. The advantages of this technique are that (a) it does not depend on angular resolution and (b) it yields straightforward empirical relationships that provide effective secondary indicators that can be used to estimate the masses of large numbers of AGNs and quasars based on single observations. The disadvantages of the technique are that (a) the accuracy of reverberation-based black hole masses are fundamentally limited by our lack of knowledge of the detailed structure and kinematics of the BLR and (b) it is observationally demanding.

Reverberation-based black hole masses are computed from the virial equation

$$M_{\text{BH}} = \frac{f R \Delta V^2}{G}, \quad (1)$$

where R is the size of the region as estimated by the mean emission-line lag τ (time delay relative to continuum variations), i.e., $R = c\tau$, ΔV is the emission-line width (preferably the width of the *variable* part of the emission line), and f is a scale factor of order unity that depends on the structure and geometry of the BLR. Two lines of evidence suggest that these masses have some validity:

1. In AGNs for which time delays have been measured for multiple lines, there appears to be a virial relationship between time delay and line width, i.e., $\tau \propto \Delta V^{-2}$ (Peterson & Wandel 1999, 2000; Onken & Peterson 2002; Kollatschny 2003).
2. In reverberation-mapped AGNs for which host galaxy bulge velocity dispersions σ_* are available, the reverberation-based masses M_{BH} are consistent with the $M_{\text{BH}} - \sigma$ relationship seen in quiescent galaxies (Gebhardt et al. 2000; Ferrarese et al. 2001; Onken et al. 2004; Nelson et al. 2004).

Reverberation mapping also shows that there is a simple relationship between the size of the BLR and the continuum luminosity L of the AGN of the form $R \propto L^\gamma$ (Kaspi et al. 2000; 2005). This is an important result, not only because it constrains the physics of the BLR, but also because it provides a secondary method of estimating the black hole masses by using L^γ as a surrogate for R in eq. (1). Since a single spectrum of an object in principle yields both L and a line width ΔV , we have a powerful tool for estimating the masses of large populations of quasars. Wandel, Peterson, & Malkan (1999) carried out some preliminary tests of this method using the $\text{H}\beta$ emission line. Vestergaard (2002; hereafter Paper I) used the $\text{C IV } \lambda 1549$ emission line to probe much higher redshifts, up to $z \approx 6$. There have been several other extensions of this methodology.

McLure & Jarvis (2002) used the $\text{Mg II } \lambda 2798$ emission line in a similar study. Wu et al. (2004) suggested that recombination-line luminosities should be used since they are a better measure of the ionizing continuum that drives the line variations than the longer-wavelength continuum, which may be contaminated by hard-to-quantify jet emission or host-galaxy starlight, depending on the wavelength at which the continuum is measured.

Since the original papers appeared, there have been a number of significant developments that have led us to decide to revisit the mass-scaling relationships based on the $\text{H}\beta$ and C IV emission lines. Specifically,

1. The reverberation-mapping database that provides the fundamental calibration for the mass-scaling relationships has been completely reanalyzed (Peterson et al. 2004). Of particular relevance here is that some inadequate or poor data were identified and removed from the database.
2. The reverberation-based masses have now been empirically scaled to the quiescent galaxy black hole mass scale through use of the $M_{\text{BH}} - \sigma$ relationship (Onken et al. 2004). The zeropoint of the AGN $M_{\text{BH}} - \sigma$ relationship was adjusted to that of quiescent galaxies by determining a mean value for the scale factor f .
3. The radius–luminosity ($R - L$) relationship between the broad-line region size and continuum luminosity has been updated based on the reanalyzed reverberation data (Kaspi et al. 2005), and new *HST* imaging of reverberation-mapped AGNs enable us to correct for host galaxy contamination of the optical continuum luminosity measured from spectra (Bentz et al. 2006).
4. Additional spectra of reverberation-mapped AGNs have become available in the public domain, making it possible to improve the calibration and better quantify the uncertainties of mass estimates based on single-epoch spectra.

In contrast to Paper I, we have also adopted the current benchmark cosmology with $H_0 = 70 \text{ km s}^{-1}\text{Mpc}^{-1}$, $\Omega_{\Lambda} = 0.7$, and $\Omega_m = 0.3$; in Paper I, we used $H_0 = 75 \text{ km s}^{-1}\text{Mpc}^{-1}$, $q_0 = 0.5$, and $\Lambda = 0$ to effect more direct comparisons of quasar luminosities with those in previous work.

In the following, we describe the data and the spectral measurements (§2), perform the calibration of the single-epoch unscaled mass estimates (§3) and determine the inherent statistical uncertainties of these relationships (§4). In §5, we briefly discuss (1) the improvements in the updated mass-scaling relationships and (2) the appropriateness of using the C IV emission line for mass estimates. Our main results are summarized in §6.

Also, there has been a controversy over the use of the C IV emission line in particular (e.g., Baskin & Laor 2005) and we wish to address that issue as well. In Appendix A, we scrutinize the data used by Baskin & Laor that led them to challenge the validity of C IV -based mass estimates and we conclude that a more suitable selection of data largely removes the problems that they

identified. Finally, in Appendix B, we provide a complete list of estimated masses for all those quasars from the Bright Quasar Survey (the Palomar–Green or “PG” quasars; Schmidt & Green 1983) for which reverberation-based masses are not available.

2. Sample and Data

We base our study on the 32 AGNs for which reliable reverberation-based mass estimates⁴ were calculated by Peterson et al. (2004); we hereafter refer to this sample as the “reverberation sample.” We obtain from independent sources emission-line widths and fluxes and continuum fluxes for these same objects and calibrate mass-scaling relationships. The 28 objects with optical spectra and the 27 objects with UV spectra that are used in this study are listed in Tables 1 and 2, respectively; column (1) of both tables gives the commonly used name of the object, and frequently used alternative names appear in column (2) of Table 1. Column (3) gives the redshift of each object.

2.1. Optical Data

Optical spectral measurements for a large fraction of the reverberation-mapped AGNs are available from large compilations by Boroson & Green (1992) and by Marziani et al. (2003). Both of these data sets are particularly suitable for determination of the $H\beta$ emission-line width because in both cases (a) the optical Fe II emission was accounted for by fitting the spectrum with a suitable template based on the spectrum of I Zw 1, and (b) an attempt was made to remove the $H\beta$ narrow-line component. In addition to the line-width measurements, we use the $H\beta$ equivalent widths from Boroson & Green (1992) and the continuum and $H\beta$ line flux densities from Marziani et al. (2003).

There is some overlap between the objects observed by Boroson & Green and Marziani et al.: specifically, of the 32 sources in the reverberation sample, 16 were observed by Boroson & Green and 28 were observed by Marziani et al. Fourteen of the sources were included in both studies, although the two studies did not always provide the same type of data. Collectively, for 25 objects in the reverberation sample, there are a total of 34 individual pairs of reliable $\text{FWHM}(H\beta)$ and $L_\lambda(5100\text{\AA})$ measurements, plus pairs of $\text{FWHM}(H\beta)$ and $L(H\beta)$ measurements for 28 objects in the reverberation sample, as listed in Table 1. These are the two optical data samples analyzed in this work. The individual measurements comprising these samples are described below.

⁴Specifically, PG 1211+143, NGC 4593, and IC 4329A were excluded from the sample of Peterson et al. (2004) on grounds of having unreliable or low-precision reverberation-based mass estimates.

2.1.1. Optical Luminosity Measurements

Continuum Luminosities. Most of the monochromatic continuum luminosities $L_\lambda(5100\text{\AA})$ for the PG quasars in the reverberation sample (14 out of 16) are computed from the specific fluxes and spectral indices measured by Neugebauer et al. (1987); in Paper I, a continuum slope of $\alpha_\nu = -0.5$, as is commonly adopted, was used instead. As in Paper I, continuum measurements for Mrk 110 and Mrk 335 are based on the B -band photometry presented by Kellermann et al. (1989) and Schmidt & Green (1983) with corrections described by Schmidt, Schneider, & Gunn (1995). Continuum luminosities for 28 of the objects (mostly Seyfert galaxies) are based on the continuum flux densities given by Marziani et al. (2003).

In Figure 1, we compare the single-epoch luminosities with the mean source luminosities of Peterson et al. (2004). The Neugebauer et al. luminosities are seen to scatter mostly within about 0.2–0.3 dex of the mean monitoring luminosities. While the Neugebauer et al. values tend to be slightly higher, the effect is minor ($\lesssim 0.1$ dex) for many objects. A similar offset was found and discussed in § 4.2 of Paper I, and was also noted by Maoz (2002). A likely cause was considered to be slightly different absolute flux calibration scales, although Maoz suggests that imperfect sky subtraction in the Neugebauer et al. data may also be a source of error. The somewhat larger aperture ($15''$) used by Neugebauer et al. compared to that used during the monitoring campaigns (typically $4''$ – $5''$) likely provides a sizable contribution to the offset. For lower luminosity objects where the relative contribution of the host galaxy is stronger, the luminosity difference is expected the largest, and indeed, the largest deviations are seen for sources with $\log L_\lambda(5100\text{\AA}) \lesssim 44.5$. The systematic offset is small and indeed is well within the envelope expected simply from source variability. We adopt these luminosities without further correction.

The spectra of Marziani et al. (2003) are not necessarily expected to be of photometric quality in part because the narrow slit ($1''.5 - 2''$) used in the observations was not always aligned at the parallactic angle and in part because of variable sky conditions. Nevertheless, we find the luminosities based on these data to be generally consistent with the monitoring data to within the factor 2 (0.3 dex) or so allowed by source variability. The spectra of the sources for which the Marziani et al. luminosities deviate by 0.3 dex or less from the mean (monitoring) luminosities are included in this study.

A correction for Galactic extinction is applied to all the flux density measurements in the observed frame of reference for each object. The extinction values we use are those listed by Kaspi et al. (2005) and are based on the Galactic extinction curve of Cardelli, Clayton, & Mathis (1989).

Line Luminosities. We determined the emission-line luminosities of the broad-line component of $H\beta$ by multiplying the equivalent width by the extinction-corrected monochromatic continuum luminosity at the position of the $H\beta$ line. This luminosity was determined by converting the observed 4861\AA flux densities provided by Marziani et al. and by extrapolating the Neugebauer et al. $L_\lambda(4416\text{\AA})$ and Schmidt & Green $L_\lambda(4400\text{\AA})$ values to 4861\AA using the continuum slopes

measured by Neugebauer et al. For the two objects with Schmidt & Green flux densities only, the average continuum slope of -0.2 measured by Neugebauer et al. for the PG sample was adopted. In the left panel in Fig. 2, we compare the values of $L(\text{H}\beta)$ determined from the Marziani et al. (2003) measurements with the mean values from the monitoring programs. We find good agreement between these two sets of measurements, with scatter consistent with intrinsic variability. However, the line luminosities based on the Boroson & Green (1992) and Neugebauer et al. (1987) data systematically overestimate the line luminosities relative to the values obtained from the monitoring data by an average of 0.28 ± 0.15 dex, i.e., almost a factor of two (Fig. 2, right). We have been unable to identify the origin of this offset, although we have been able to eliminate some of the more obvious potential sources of error, such as the above mentioned extrapolation of the continuum from 4416 \AA or 4400 \AA to $\text{H}\beta$ (maximum effect less than 0.05 dex). Given this lack of agreement, we omit the data shown in the right diagram in Fig. 2 from further consideration.

We give the extinction-corrected 5100 \AA continuum luminosities $\lambda L_{\lambda}(5100 \text{ \AA})$ and line luminosities $L(\text{H}\beta)$ in columns (6) and (7), respectively, of Table 1. Uncertainties in flux densities are taken directly from Neugebauer et al. (1987) when available, and errors are propagated assuming that the uncertainties in the spectral slopes are $\sigma(\alpha) = 0.2$ (see Paper I). In the case of the Marziani et al. (2003) data, we estimated the uncertainty in the flux from their quoted signal-to-noise ratios. In the case of the PG quasars not observed by Neugebauer et al., the B -band magnitude uncertainty of 0.27 mag (Schmidt & Green 1983) is adopted.

2.1.2. $\text{H}\beta$ Line Width Measurements

For the PG objects, we use the $\text{FWHM}(\text{H}\beta)$ measurements of the broad-line component from Boroson & Green (1992), except for the corrected value for PG 1307+085 ($\text{FWHM} = 5320 \text{ km s}^{-1}$) from Laor (2000). Broad-component widths were also taken from Marziani et al. (2003). In Fig. 3, we show that for the objects common to both studies the FWHM measurements of the Boroson & Green and the Marziani et al. studies are consistent within the errors. The circled data points are those for which the Marziani et al. luminosities differ from those measured during the reverberation-mapping monitoring program by less than 0.3 dex. We are thus reassured that larger changes in luminosity do not strongly affect the line width.

We note an important change from Paper I is that we now measure the width of the broad component only⁵.

We correct the line width measurements for spectral resolution following the procedure of Peterson et al. (2004). For the Boroson & Green (1992) measurements, we adopt a value of the

⁵In Paper I, we noted that the narrow-component of $\text{H}\beta$ did not vanish in the rms spectrum formed from the monitoring data in the case of PG 1704+608 (Kaspi et al. 2000); it is now clear that this result was spurious (see Boroson 2003; Peterson et al. 2004).

spectral resolution of $\text{FWHM} = 7 \text{ \AA}$. The resolution of each of the Marziani et al. (2003) spectra is given in Table 1 of their paper.

The FWHM line width of $\text{H}\beta$, corrected for spectral resolution, is listed in column (4) of Table 1. Measurement uncertainties for the FWHM values are not quoted by Boroson & Green (1992) or Marziani et al. (2003) and therefore a 10% error is adopted, similar to our approach in Paper I; this is likely a lower limit, especially for low values of FWHM.

2.2. UV Data

We retrieved all the UV spectra of the 32 reverberation sample AGNs that were available as of 2004 May from the *IUE*, *HUT*, and *HST* archives; one source (PG 0844+349) has no C IV data in the archives and another four objects (PG 0804+761, NGC 3227, PG 1411+442, PG 1700+518) were later omitted (see § 2.2.3), leaving a final sample of 27 objects with UV data. We processed and measured each spectrum to ensure that the data were treated in a consistent manner. *IUE* spectra of AGNs are of widely varying quality owing to the small size of the telescope and limitations of the detector; quasar spectra, in particular, can often be of low quality. We therefore use *IUE* spectra of only the brighter AGNs and quasars in this analysis (Table 2). Of the *HUT* spectra available in the MAST⁶ archives, only those we deem to be of sufficient quality are selected. The spectra are corrected as needed for photometric calibration following the prescription at the *HUT* website⁷.

The *HST* spectra were observed with a variety of grating settings and we reprocessed only those covering the C IV region of each spectrum. For PG 0953+414 and 3C 273 some of the FOS spectra were obtained in “rapid” mode (45 and 384 spectra, respectively), that is, all the individual subexposures of a given observation are preserved and a final combined spectrum is yet to be produced. For these spectra obtained in “rapid” mode, the individual spectra are thus extracted and combined, weighted by their variance spectra so to maintain their optimal signal-to-noise ratio; this procedure is analogous to that described by Horne (1986). For each object in our sample, spectra obtained on the same day that show no significant differences in continuum level or line profile are similarly combined by variance weighting. In a few cases, especially for *IUE* data, spectra spanning weeks to months with no noticeable difference in continuum level or line profile are similarly combined. Specific potentially problematic data sets that are flagged or omitted are briefly discussed in § 2.2.3.

The final sample of 27 objects for which the UV spectra retrieved from the public archives are used in this study are listed in column (1) of Table 2. Column (2) lists the date of observation, column (3) gives the redshift, and column (4) lists the telescope and instrument used. Owing to the availability of multiple spectra for many of the objects, we have a total of 85 individual estimates

⁶Multi-Mission Archive at Space Telescope; <http://archive.stsci.edu/>.

⁷<http://archive.stsci.edu/hut>

of black hole masses.

2.2.1. *UV Continuum Luminosities*

We fitted the rest-frame UV spectra with a power-law continuum in nominally line-free windows typically in the wavelength ranges 1265 – 1290 Å, 1340 – 1375 Å, 1425 – 1470 Å, 1680 – 1705 Å, and 1950 – 2050 Å, but slightly adjusted interactively for each individual spectrum in order to avoid broad absorption features or extended wings of emission lines; the fitting algorithm we employed automatically excludes strong, narrow absorption lines. We computed the root-mean-square (rms) continuum flux density (hereafter simply called “continuum rms”) relative to the best-fit continuum within the continuum windows. In addition to the best-fit continuum, we also generated four extreme continua using the best fit continuum and the continuum rms: a high-level continuum, a low-level continuum, and two continua with extreme blue and red slopes. These four extreme continuum settings were used to estimate uncertainties in the line measurements ascribable to the choice of continuum; this is typically the largest source of error in AGN spectral analysis, but is seldom well-quantified. The uncertainty in the line-width measurement is of particular importance in this context on account of the sensitivity of the inferred black hole masses to the line width measurements.

We compute monochromatic continuum luminosities $L_{\lambda}(1350\text{Å})$ and $L_{\lambda}(1450\text{Å})$ for each spectrum from the observed continuum flux density of the best-fit continuum. The uncertainty in the continuum luminosity is determined from the continuum rms. The luminosities are extinction-corrected in the same manner as the optical luminosities discussed earlier. Figure 4 shows that the $L_{\lambda}(1350\text{Å})$ and $L_{\lambda}(1450\text{Å})$ values are essentially the same to within the uncertainties, so we list only the single-epoch $\lambda L_{\lambda}(1350\text{Å})$ values in column (8) of Table 2.

2.2.2. *CIV Line Width Measurements*

We measured two line-width parameters, FWHM and line dispersion σ_l , using the methodology described by Peterson et al. (2004), in particular to deal with double-peaked emission lines⁸. For practical purposes, the line limits for σ_l , the second moment of the emission-line profile, are set to $\pm 10,000\text{ km s}^{-1}$ of the rest-frame line center, since in every case either the profile and the best-fit continuum merged between $\sim 9,000\text{ km s}^{-1}$ and $10,000\text{ km s}^{-1}$ or the N IV] $\lambda 1486$ line contributes blueward of $-10,000\text{ km s}^{-1}$ from the CIV profile center. For spectra with a strong contribution from He II $\lambda 1640$ the observed CIV red wing lies above the best-fit continuum. A red wing limit

⁸Peterson et al. (2004) note a number of advantages to using σ_l rather than FWHM as the line-width measure. We did not do this here with H β because we are relying completely on published line measurements, which only give FWHM. An H β mass-scaling relationship based on σ_l will be explored in a separate paper.

of $10,000 \text{ km s}^{-1}$ is adopted nonetheless based on the assumption that this provides a reasonable compromise estimate of the red wing flux, some of which will extend into and blend with the blue wing of He II which also may contribute a fraction of the flux in the extreme red wing of C IV; the $10,000 \text{ km s}^{-1}$ mark falls approximately halfway between the C IV and He II lines. For those spectra, the line flux and line dispersion may be slightly overestimated, especially if Fe II emission is present (Marziani et al. 1996).

Some of the objects have absorption superposed on the C IV emission lines. We experimented with different ways of correcting for mild absorption in the profile and concluded that a simple interpolation across the absorption does a reasonably good job of approximating the (non-absorbed) line profile, as long as the absorption is not too close to the line center. We discarded from the sample objects for which the absorption is so strong that it is clear that a simple interpolation is misleading (see § 2.2.3).

Both of the line width parameters were measured relative to each of the five continuum settings described above. We adopt the line width measurements based on the best-fit continuum. We then compute the difference between this measurement and the other four and, to be conservative, adopt as the uncertainty the largest difference.

For consistency, we correct the line-width measurements for spectral resolution effects in the same manner as the optical measurements (following Peterson et al. 2004), even though the corrections are typically insignificant for the high-resolution *HST* and *HUT* data. We adopt a resolution of $\text{FWHM} = 6 \text{ \AA}$ for the *IUE* spectra⁹. The MAST web page¹⁰ gives $\text{FWHM} = 3 \text{ \AA}$ for *HUT1* spectra and 2 \AA at 1600 \AA for the *HUT2* spectra. Based on the *HST* FOS Handbook¹¹, the approximate resolution of both pre-costar and post-costar spectra were estimated for each of the G130H, G190H, and G270H gratings. These estimates are generally consistent with an average FOS resolution of 1.9 \AA (across the three grating spectra) adopted by Peterson et al. The *HST* GHRS spectral resolution was likewise estimated to be 0.65 \AA for the G140L grating. The spectral resolution of *HST* STIS spectra vary with the specific instrument configuration. The resolution adopted for each UV spectrum is listed in column (5) of Table 2. The resolution-corrected $\text{FWHM}(\text{C IV})$ and $\sigma_l(\text{C IV})$ values are listed in columns (6) and (7), respectively.

2.2.3. Flagged and Omitted Data Sets

Flagged Data. Data sets that we consider to be of questionable or marginal quality are flagged so to check whether they distribute differently than the higher-quality data. The flagged data sets

⁹The resolution of the SWP *IUE* spectra is listed on the MAST web page: <http://archive.stsci.edu/iue/>.

¹⁰<http://archive.stsci.edu/hut>

¹¹http://www.stsci.edu/hst/HST_overview/documents

are marked in column (11) of Table 2. The three *IUE* spectra of Mrk 79 are of borderline quality. The NGC 3516 *HST* spectrum of 1996 November 28 exhibits a large deviation in the unscaled mass estimate ($v^2 R \propto \text{FWHM}^2 L^\gamma$, where γ is the slope of the $R - L$ relationship) from the remaining data sets for unknown reasons. The PG 0026+129 *HST* spectrum has an odd appearance and this data point is an outlier relative to the cluster of PG quasars. As there is only one spectrum available of this source, and we have no independent means of assessing the quality of these data, we leave this data point in the database, but flag it. The *IUE* spectrum of PG 1617+175 is of marginal quality, but the large uncertainties we find seem to be commensurate with the data quality. Given the low number of luminous quasars in our sample, this data point is not omitted, but flagged.

Omitted Data. For PG 0804+761, only *IUE* data are available, but the quality is very poor and this target was thus excluded. In spite of the good quality of the *HST* spectrum of NGC 3227 (Crenshaw et al. 2001), these data are omitted from the analysis owing to the strong internal reddening in this source, which cannot be reliably corrected and which affects the spectral measurements (see also Kaspi et al. 2005). The *IUE* spectra of NGC 4051 are omitted as the spectral resolution is too low for objects with such strong absorption features; the *IUE* line profiles are not representative of the intrinsically emitted profiles. We use the *HST* echelle spectrum of NGC 4051 (Collinge et al. 2001) instead. For NGC 4151, the *HUT* spectrum of 1990 December 8 is contaminated by a high background, rendering the data unusable. The 2000 May 28 *HST* spectrum was obtained during a very low-luminosity state of NGC 4151. At this flux state the low resolution of the G140L grating does not allow the C IV profile to be well defined owing to the strong absorption in the blue profile wing. The *HUT* spectra, and the 1992 April, 1992 May, and 1995 December 18 *IUE* spectra of 3C 273 are of insufficient quality. While PG 1411+442 was observed with both *IUE* and *HST*, strong absorption centered on the C IV profile render the data unusable for our purposes. Similarly, PG 1700+518 is excluded as it is a broad absorption-line quasar.

3. Calibration of Single-Epoch Mass Estimates

As in Paper I, we calibrate the single-epoch mass estimate by using the reverberation-based mass measurements. We compute for each spectrum (i.e., for each single epoch) a measure of the unscaled mass μ defined as the product

$$\mu = \left(\frac{\Delta V}{1000 \text{ km s}^{-1}} \right)^2 \left(\frac{\lambda L_\lambda}{10^{44} \text{ erg s}^{-1}} \right)^\gamma \quad (2)$$

where ΔV is the line-width measurement (either FWHM or σ_l) for either C IV $\lambda 1549$ or H β , γ is the slope of the relevant $R - L$ relationship, and L_λ is the continuum luminosity (at either 1350 Å or 5100 Å). We will also use the broad component of H β itself as a luminosity measure, i.e.,

$$\mu = \left(\frac{\text{FWHM}(\text{H}\beta)}{1000 \text{ km s}^{-1}} \right)^2 \left(\frac{L(\text{H}\beta)}{10^{42} \text{ erg s}^{-1}} \right)^\gamma. \quad (3)$$

The unscaled mass estimate μ should be proportional to the black hole mass (eq. 1) obtained by reverberation mapping $M_{\text{BH}}(\text{RM})$. We thus first check this assumption, because if it holds, the problem of calibrating the unscaled masses reduces to a simple relationship with only one degree of freedom,

$$\log M_{\text{BH}}(\text{RM}) = \log \mu + a. \quad (4)$$

Following Paper I, the constant zero-point offset a between the unscaled mass estimate and the black hole mass is thus the weighted average of the difference between these two measures obtained for each spectrum of each object.

We use two independent algorithms, FITEXY (Press et al. 1992) and BCES (Akritas & Ber-shady 1996), in our regression analysis. Since the error bars in the reverberation-mapping mass estimates are often asymmetric, we adopt the same method as Kaspi et al. (2005) of using the error value for a given point that is in the direction of the best-fit line. This requires a few iterations of the regression analysis and the error selection (i.e., either the positive or the negative error). We incorporate intrinsic scatter in the FITEXY relationships in the same way as Kaspi et al. (2005).

3.1. Radius – Luminosity Relationships

Kaspi et al. (2005) recently updated the $R - L$ relationships for the Balmer lines based on the revised and improved reverberation database of Peterson et al. (2004). Kaspi et al. also used the same fitting algorithms that we use here, which give slightly different results from one another on account of slightly different underlying assumptions. Since both methods have merit and one is not obviously more appropriate than the other, we form a weighted average of the slopes γ obtained from the FITEXY and BCES regressions. In each case, we conservatively adopt a final uncertainty in the exponent of $\Delta\gamma = 0.06$, which is typical of the maximum differences in the index γ yielded by the two algorithms and slightly larger than the typical uncertainty resulting from the individual algorithms and the errors on the weighted mean slopes (i.e., $\sigma(\gamma) \approx 0.03\text{--}0.05$).

For the relationship between $\text{H}\beta$ radius and the optical continuum, we use the Kaspi et al. FITEXY and BCES slopes based on each individual reverberation measurement of the $\text{H}\beta$ line for all AGNs in the sample, and modified by Bentz et al. (2006) to include corrections for host galaxy stellar light contribution to the $L_{\lambda}(5100\text{\AA})$ values for most of the low-luminosity AGNs in the sample, i.e., $R \propto L_{\lambda}(5100\text{\AA})^{0.50 \pm 0.06}$. Use of the alternative bases (e.g., the results based on averaging all results for a single object) changes the results only slightly.

For the relationship between the $\text{H}\beta$ radius and the $\text{H}\beta$ broad component luminosity, we use $R \propto L(\text{H}\beta)^{0.63 \pm 0.06}$, based on the Kaspi et al. (2005) results as explained above.

For the relationship between the $\text{H}\beta$ radius and the UV continuum luminosity, we use $R \propto L_{\lambda}(1350\text{\AA})^{0.53 \pm 0.06}$, and note that use of $L_{\lambda}(1450\text{\AA})$ instead of $L_{\lambda}(1350\text{\AA})$ gives an identical result. We also note that $\gamma = 0.53$ is a distinctly shallower slope than we used in Paper I ($\gamma = 0.7$), but is

much closer to that expected for a photoionized BLR (see below).

Selecting a slope to use for the C IV $R - L$ relationship is more difficult because there are so few actual measurements of the C IV response time and most of these measurements are over a very narrow range in luminosity. Recently, however, Peterson et al. (2005) measured the C IV response in NGC 4395, the least luminous known Seyfert 1 galaxy. This result shows that the size of the C IV emitting region is about as expected if the $R(\text{C IV}) - L_\lambda(1350 \text{ \AA})$ relationship has a slope similar to that of $R(\text{H}\beta) - L_\lambda(1350 \text{ \AA})$. Peterson et al. find that the slope of C IV $R - L$ relationship to be $\gamma = 0.61 \pm 0.05$, although this result is based heavily on the NGC 4395 reverberation measurement¹². The C IV slope is generally consistent with the slope of the $R(\text{H}\beta) - L_\lambda(1350 \text{ \AA})$ relationship, $\gamma = 0.56 \pm 0.05$ (Kaspi et al. 2005), as well as the relationship between $R(\text{H}\beta)$ and the starlight-corrected optical luminosity $L_\lambda(5100 \text{ \AA})$, $\gamma = 0.54 \pm 0.04$ (Bentz et al. 2006).

3.2. Optical Mass Relationships

There are two luminosity surrogates for R in the optical regime, the 5100 \AA continuum luminosity $L_\lambda(5100 \text{ \AA})$ and the $\text{H}\beta$ line luminosity $L(\text{H}\beta)$. The associated unscaled masses $\mu[\text{FWHM}(\text{H}\beta), L_\lambda]$ and $\mu[\text{FWHM}(\text{H}\beta), L(\text{H}\beta)]$ are computed according to eqs. (2) and (3), respectively. In Fig. 5, we compare directly our single-epoch unscaled mass estimates with the calibrated black hole masses determined by reverberation mapping, and we perform a regression analysis on these data, the results of which are given in Table 3. In the case of the BCES regressions, we list only the bootstrapped bisector slopes, intercept, and related errors as these results are relatively insensitive to outliers. A few thousand realizations have been made in each regression analysis. For the FITEXY regressions, we apply for convenience an equal amount of intrinsic scatter to both the masses from reverberation mapping $M_{\text{BH}}(\text{RM})$ and the single-epoch unscaled mass estimates μ . The level of scatter needed to obtain a reduced χ^2 value of unity is a little higher ($\sim 50\%$) than obtained by Kaspi et al. (2005) for the $R - L$ relationships ($\sim 40\% - 45\%$), but is consistent. The increased level of scatter obtained for the mass relationships is entirely expected because single-epoch spectra are not necessarily obtained in an average state, which the reverberation mapping data somewhat represent. Both unscaled mass estimates are strongly correlated with the black hole masses with a regression slope consistent with a value of 1.0 to within the quoted uncertainties. The scatter in the relationships is similar.

The excellent correlation between $M_{\text{BH}}(\text{RM})$ and μ justifies the use of eq. (4), thus requiring only that we establish the offset between these two quantities. The results are listed in Table 4. The calibrated single-epoch black hole mass estimates based on the unscaled masses $\mu[\text{FWHM}(\text{H}\beta), L_\lambda]$ or $\mu[\text{FWHM}(\text{H}\beta), L(\text{H}\beta)]$, are listed in columns (9) and (10), respectively, of Table 1. The reverberation-based black hole mass measurements used to effect this calibration are

¹²This value of the slope of the C IV $R - L$ relationship appears in an erratum to this paper.

listed in column (11).

3.3. UV Mass Relationships

In the UV regime, we have two measures of the line width, FWHM and σ_l . We therefore have two separate sets of μ values to calibrate. The zero-point of these unscaled mass estimates is not expected to be the same (e.g., Onken et al. 2004; Peterson et al. 2004). In addition, the sample of UV measurements is so large that it is worth testing whether we get a significantly different result if the weighted mean of the individual measurements obtained at different epochs are analyzed instead. This approach is similar to that adopted by Kaspi et al. (2005). When computing the mean weighted by the measurement uncertainties, we exclude the few (7) entries that are based on mean data of monitoring campaigns (marked in Table 2) owing to the unnecessary complications involved in computing the true weighted mean if they are included. The unscaled mass estimates based on the mean monitoring data are included in the analysis as seven separate data points; hence the full sample of weighted averages counts 34 entries.

In Fig. 6, we compare the unscaled mass estimates $\mu[\text{FWHM}(\text{C IV}), L_\lambda(1350\text{\AA})]$ (hereafter $\mu[\text{FWHM}(\text{C IV})]$; eq. 2) determined from the full sample of individual entries (left panel) and the sample of weighted averages (right panel) with the reverberation-based masses. The low-luminosity Seyfert NGC 4051 is labeled. Flagged objects (§2.2.3) are marked by red circles and objects with mild absorption corrected for in the C IV line profile are marked with blue triangles. In both cases, the unscaled mass correlates well with the black hole mass. In addition, neither the flagged nor marked objects are conspicuous outliers, and therefore none of these measurements will be omitted from the analysis. These regression results are also listed in Table 3. We note in particular that the relationship between $\mu[\text{FWHM}(\text{C IV})]$ and the reverberation-based masses is consistent with a linear relationship. The uncertainty in the fitted slope is higher for the sample based on weighted means, and the estimated intrinsic scatter increases from 42% to $\sim 52\%$. Given the somewhat isolated position of NGC 4051, we repeated the regression analysis with this source omitted to test the sensitivity of the regression fits to this data point. The sample of weighted means is more sensitive to whether or not NGC 4051 is included, but in neither case does the slope deviate from a value of unity by more than 2σ .

We repeat this analysis for the UV unscaled mass based on the C IV line dispersion $\mu[\sigma_l(\text{C IV}), L_\lambda(1350\text{\AA})]$ (hereafter $\mu[\sigma_l(\text{C IV})]$, eq. 2) instead of FWHM. We compare the unscaled masses $\mu[\sigma_l(\text{C IV})]$ and reverberation-based masses in Fig. 7 for both the sample of individual measurements (left panel) and the sample of weighted means (right panel). Again, the measurements exhibit a strong correlation with similar scatter in the two samples and the flagged measurements show no particular bias. The BCES regression slopes are also here consistent with a slope of unity, typically to within 1σ .

In this case, the FITEXY regression analysis yields slopes that tend to be steeper than unity,

but are nevertheless consistent with a value of unity to within 3σ . The estimated intrinsic scatter is here some 10% lower than for the $\mu[\text{FWHM}(\text{C IV})]$ relationship. Again, the weighted mean sample tends to yield steeper slopes than those of the sample of individual measurements, especially when NGC 4051 is excluded, but the errors are correspondingly larger.

Since each of the BCES and FITEXY regression fits are consistent with one another and with a linear relationship between the unscaled single-epoch mass estimates and the reverberation-based masses, we again conclude that it is appropriate to estimate the black hole mass through eq. (4) and that all we need to do is establish the offset a . The zero-points and errors we compute are listed in Table 4. The final calibrated single-epoch black hole mass estimates based on $\text{FWHM}(\text{C IV})$ and on $\sigma_l(\text{C IV})$ are listed in columns (9) and (10) of Table 2, respectively.

3.4. Summary of the Calibrated Mass Scaling Relationships

We conclude this section with a summary of the mass-scaling relationships for obtaining black hole masses estimates from single-epoch spectra.

1. **$\text{FWHM}(\text{H}\beta)$ and $L_\lambda(5100 \text{ \AA})$.** For the optical continuum luminosity and FWHM of the $\text{H}\beta$ broad component,

$$\log M_{\text{BH}}(\text{H}\beta) = \log \left[\left(\frac{\text{FWHM}(\text{H}\beta)}{1000 \text{ km s}^{-1}} \right)^2 \left(\frac{\lambda L_\lambda(5100 \text{ \AA})}{10^{44} \text{ erg s}^{-1}} \right)^{0.50} \right] + (6.91 \pm 0.02). \quad (5)$$

The sample standard deviation of the weighted average zeropoint offset, which shows the intrinsic scatter in the sample, is ± 0.43 dex. This value is more representative of the uncertainty in the zero-point than is the formal error.

2. **$\text{FWHM}(\text{H}\beta)$ and $L(\text{H}\beta)$.** For the $\text{H}\beta$ broad-component luminosity and FWHM,

$$\log M_{\text{BH}}(\text{H}\beta) = \log \left[\left(\frac{\text{FWHM}(\text{H}\beta)}{1000 \text{ km s}^{-1}} \right)^2 \left(\frac{L(\text{H}\beta)}{10^{42} \text{ erg s}^{-1}} \right)^{0.63} \right] + (6.67 \pm 0.03). \quad (6)$$

The sample standard deviation of the weighted average zeropoint offset is ± 0.43 dex.

3. **$\text{FWHM}(\text{C IV})$ and $L_\lambda(1350 \text{ \AA})$.** For the ultraviolet continuum luminosity and the FWHM of the C IV line,

$$\log M_{\text{BH}}(\text{C IV}) = \log \left[\left(\frac{\text{FWHM}(\text{C IV})}{1000 \text{ km s}^{-1}} \right)^2 \left(\frac{\lambda L_\lambda(1350 \text{ \AA})}{10^{44} \text{ erg s}^{-1}} \right)^{0.53} \right] + (6.66 \pm 0.01). \quad (7)$$

The sample standard deviation of the weighted average zeropoint offset is ± 0.36 dex.

4. $\sigma_l(\text{C IV})$ and $L_\lambda(1350 \text{ \AA})$. For the ultraviolet continuum luminosity and the dispersion of the C IV emission line,

$$\log M_{\text{BH}}(\text{C IV}) = \log \left[\left(\frac{\sigma_l(\text{C IV})}{1000 \text{ km s}^{-1}} \right)^2 \left(\frac{\lambda L_\lambda(1350 \text{ \AA})}{10^{44} \text{ erg s}^{-1}} \right)^{0.53} \right] + (6.73 \pm 0.01). \quad (8)$$

The sample standard deviation of the weighted average zeropoint offset is ± 0.33 dex.

As noted earlier, the $L_\lambda(1450 \text{ \AA})$ luminosity can be straightforwardly be substituted for $L_\lambda(1350 \text{ \AA})$ without error or penalty in precision.

4. Accuracy of the Estimated Masses

Following the approach of Paper I, we use simple counting statistics to evaluate the *statistical* uncertainty in the calibrated mass-scaling relationships. In Figs. 8 and 9, we show the deviations of the calibrated single-epoch optical and UV mass estimates (eqs. 5 – 8) from the reverberation-based black hole mass as a function of the mass. The typical dispersion of the distributions of optical mass estimates is about 0.5 dex. The UV single-epoch mass estimates exhibit a slightly larger range in deviations, but all measurements remain within 1 dex of the reverberation masses (Fig. 9).

In Table 5, we show the probability that mass estimates based on eqs. (5) – (8) will reproduce the reverberation-based mass to a specified level of accuracy. Table 5 also lists the 1σ and 2σ uncertainties in the mass estimates for each mass-scaling relationship. We see that there is a fairly high probability that the mass estimates are good to within a factor of about 3. Interestingly, the UV relationships have a slightly higher probability ($\sim 85\%$) of being accurate to a factor 3 than do the optical relationships ($\sim 70\%$), while the latter show no objects deviating by a factor 6 or more, contrary to the UV relationships. This is also reflected in the scatter around zero deviation: the UV relationships display a 1σ scatter of only ~ 0.3 dex, while the optical relationships have a 1σ scatter of ~ 0.5 dex.

One source of additional scatter in the optical relationship is contamination of the single-epoch $L_\lambda(5100 \text{ \AA})$ by host galaxy light. This is typically strongest for the lower luminosity AGNs but is not corrected for in the single-epoch luminosities on the grounds that for typical applications of this relationship a correction for host galaxy light, which requires additional data and non-trivial analysis, will not commonly be performed. The error made in not correcting for the host galaxy luminosity will be explored elsewhere.

An important point to make is that this discussion refers to how accurately the mass-scaling laws reproduce the reverberation-based masses. The reverberation-based masses are themselves uncertain typically by a factor of ~ 2.9 , based on the scatter of the reverberation-based masses around the $M_{\text{BH}} - \sigma$ relationship (Onken et al. 2004). To obtain the absolute uncertainties, we need to fold in the absolute accuracy of the reverberation mapping-mass measurements, and these values

are given in column (7) of Table 5. We estimate that the absolute accuracy of the single-epoch mass estimates range between a factor 3.6 and 4.6.

In closing, it is worth re-emphasizing that these uncertainties are only of statistical nature; any given estimate from a mass-scaling relationship can be off by up to an order of magnitude and should not be trusted in applications where high accuracy is critical. These mass estimates are, however, suitable for application to large statistical samples.

5. Discussion

In Paper I, we found that the predominant source of scatter in the mass-scaling relationships is traceable to the relatively large scatter in the $R - L$ relationship (Kaspi et al. 2000). The recent improvements in both the $R - L$ relationships (Kaspi et al. 2005) and in the reverberation-based mass measurements (Peterson et al. 2004) have correspondingly decreased the scatter in the mass estimates, at least for the estimates based on UV data. The 1σ scatter is now only a factor of about 2, compared to the factor of 3.2 found in Paper I. Implicit in this estimate is that the reverberation-mapped AGNs are reasonably representative of the AGN and quasar population as a whole.

It appears that no improvement has been achieved for the optical relationship based on $\text{FWHM}(\text{H}\beta)$ and $L_\lambda(5100 \text{ \AA})$. However, this relationship was, in fact, *not calibrated* in Paper I; the single-epoch estimates based on the relationships quoted by Kaspi et al. (2000) were merely confirmed to be consistent with the reverberation-based masses. In the current calibration, these optical mass estimates now distribute more evenly around zero offset (Fig. 8, left panel) compared to those of Paper I (cf. Fig. 6a in Paper I).

There are a number of advantages to the use of the C IV line width as a mass indicator (eq. 7), as argued in Paper I and by Warner, Hamann, & Dietrich (2003) and Vestergaard (2004). It has been argued, however, that C IV may be an inappropriate choice for this application on the grounds that the dynamics of the C IV-emitting gas may not be determined primarily by gravitation; in particular, it has been suggested (1) that the line profiles might be affected by obscuration within the line-emitting region, and (2) that there are reasons to believe that a significant fraction of the C IV line arises in an outflowing wind. We address these two issues in turn.

Richards et al. (2002) used a large sample of SDSS quasars to investigate the observed blueshift of the peak of the C IV profile relative to the low-ionization lines, which is a well-known phenomenon (e.g., Gaskell 1982; Wilkes 1984; Tytler & Fan 1992). They suggest that the apparent blueshift may actually be a lack of emission in the red profile wing, suggestive of occultation or obscuration, i.e., a non-gravitational alteration of the profile. Richards et al. divide their database into four groups based on the magnitude of the C IV blueshifts (their Fig. 5 and Table 2) and form composite spectra for each of these subsets. They find that the most blueshifted profile typically has $\text{FWHM}(\text{C IV}) = 1600 \pm 300 \text{ km s}^{-1}$, which is only 15% broader than the C IV profile from the least blueshifted

composite. There is thus a bias in the sense that the subset with the most strongly affected profiles will have masses overestimated by $\sim 30\%$. However, this effect is considerably smaller than the typical uncertainties even in the reverberation-based masses, which as noted earlier are uncertain by a factor of ~ 2.9 (Onken et al. 2004).

It is sometimes stated (e.g., Dunlop 2004; Bachev et al. 2004; Shemmer et al. 2004; Baskin & Laor 2005) that the C IV profile is unsuitable for estimating AGN black hole masses from single-epoch spectra because the component of C IV that arises in an outflowing wind, as is the case with other higher-ionization lines, is much more significant than in, say, lower ionization lines such as Mg II or H β . The C IV profile of some narrow-line Seyfert 1 galaxies (NLS1s) may contain a significant contribution from a wind, and indeed Vestergaard (2004) cautioned against using C IV to estimate the masses of black holes in this type of object. It should be pointed out, however, that not all NLS1s exhibit this behavior. But there does seem to be a tendency for higher-luminosity NLS1s to exhibit more highly asymmetric profiles (Leighly 2000), and there is thus a concern that the masses of luminous quasars may be overestimated by failing to account for a strong wind contribution. Vestergaard (2004) examined in detail the C IV line asymmetries of high-luminosity quasars in the range $1.5 \leq z \leq 5$ and found that none of the profiles resembled in any way the triangular shape seen in the spectra of some luminous NLS1 galaxies, like I Zw 1 (e.g., Vestergaard & Wilkes 2001). Also, such profiles are not seen by Richards et al. (2002). With a conservative selection of objects with possible blue wing asymmetries, Vestergaard (2004) determined the typical mass and luminosity of the quasars with and without these asymmetries and found insignificant differences between the two subsets.

Baskin & Laor (2005) find that the C IV equivalent width $EW(C\text{ IV})$ correlates with the Eddington luminosity ratio computed from the H β -based masses, $L_{\text{bol}}/L_{\text{Edd}}(H\beta)$. Since they do not find a similarly strong correlation between $EW(C\text{ IV})$ and $L_{\text{bol}}/L_{\text{Edd}}(C\text{ IV})$ for their sample of BQS sources, they argue that the C IV profile may yield biased black hole mass estimates. As described in Appendix A, we have undertaken a reanalysis of the Baskin & Laor sample in which we removed (a) the NLS1s, (b) low-quality *IUE* spectra of PG quasars, (c) objects with strong absorption near the C IV emission-line peak, and (d) measurements based on what we consider to be a dubious assumption about a narrow-line component of the C IV emission line, and we find that the problems cited by Baskin & Laor are much less severe. The remaining C IV FWHM values scatter within ± 0.2 dex of $FWHM(H\beta)$, thereby showing reasonable consistency. This result is also consistent with that of Warner et al. (2003), who find, on average, reasonable agreement between the mass estimates based on H β and those based on C IV.

Indeed, the most compelling reason to have some confidence in the C IV-based mass estimates is because in the handful of objects in which reverberation results are available for multiple emission lines, the virial products are consistent for *all* the measured emission lines, including C IV (Peterson & Wandel 1999, 2000; Onken & Peterson 2002).

6. Summary

We present improved relationships between spectrophotometric parameters, specifically luminosities and emission-line widths, that allow us to estimate the masses of the central black hole in AGNs. The calibration of these relationships is based on reverberation results for 32 AGNs. These relationships allow black hole mass estimates of large samples of AGNs to be obtained easily and within a short period of time and are thus particularly useful for distant AGNs and quasars where more direct mass measurement techniques are impractical or unfeasible.

The new mass-scaling relationships, presented here in § 3.4, supersede those presented by Kaspi et al. (2000), Vestergaard (2002; Paper I), and Wu et al. (2004) on account of significant improvements, beginning with the reanalysis of the reverberation database (Peterson et al. 2004), which yield improved BLR sizes and masses. Also, the reverberation-based mass scale has now been empirically calibrated for the first time through the $M_{\text{BH}} - \sigma$ relationship (Onken et al. 2004), the BLR $R - L$ relationships have been recomputed (Kaspi et al. 2005; Bentz et al. 2006), and there are more and better optical and UV spectra available to establish these scaling laws and assess their uncertainties. Moreover, these mass-scaling relationships have also been updated to the current Λ CDM benchmark cosmology.

The updated mass-scaling relationships show considerable improvement in the internal scatter compared to the same relationships in Paper I. The 1σ uncertainty is of order of a factor of 2 to 2.5 relative to the reverberation-based masses and we estimate that the absolute accuracy of the masses from the scaling relationships is a factor of ~ 4 (Table 5). We emphasize, however, that the uncertainties quoted here are only applicable to statistical samples. The uncertainty associated with a single mass estimate may be much higher; possibly these relationships may only yield order of magnitude mass estimates for individual measurements.

The anonymous referee is thanked for careful reading of the manuscript and for helpful comments. We are grateful for support of this research through grant HST-AR-10691 from NASA through the Space Telescope Science Institute, which is operated by the Association of Universities for Research in Astronomy, Incorporated, under NASA contract NAS5-26555, and through grant AST-0205964 from the National Science Foundation. The optical and UV *HST* STIS spectra of NGC 3227 and NGC 4051 and the STIS echelle spectrum of NGC 4051 were all kindly provided by Mike Crenshaw. Table 1 of Baskin & Laor (2005) was kindly provided in electronic form by Alexei Baskin. This research has made use of the NASA/IPAC Extragalactic Database (NED) which is operated by the Jet Propulsion Laboratory, California Institute of Technology, under contract with the National Aeronautics and Space Administration.

A. Reanalysis of Baskin & Laor Data

As noted in §5, Baskin & Laor (2005) caution against the use of the C IV emission line for estimating black hole masses through mass-scaling relationships of the type derived in this paper. As their conclusion was contrary to that reached in Paper I and by Warner et al. (2003) and Vestergaard (2004), we felt that it was important for us to examine the same data as Baskin & Laor and attempt to understand the origin of these different results.

Fundamentally, Baskin & Laor (2005) were concerned about apparent differences between the profiles of H β and C IV. To compare these profiles for a large number of objects, they used data on 81 of the 87 BQS (PG) quasars from the study of Boroson & Green (1992). The C IV profile measurements were based on *HST* FOS and *IUE* archival spectra, and these were compared with the H β measurements from Boroson & Green. For the purpose of this discussion, their main conclusions were (1) that FWHM(C IV) is not always larger than FWHM(H β) as expected if C IV is emitted closer to the center than H β which photoionization models and monitoring data indicate, and (2) that “C IV appears to provide a less accurate and possibly biased estimate of the black hole mass in AGNs, compared to H β .”

Upon investigating this issue ourselves, we have concluded that the poor correlation between FWHM(C IV) and FWHM(H β) that concerned Baskin & Laor (2005) is due in large part to the database they used, both in terms of sample bias and screening of sources and secondarily to their assumption about a C IV narrow component.

The first problem is inclusion of NLS1s and similar AGNs in the Baskin & Laor (2005) sample¹³. There are 17 NLS1s and narrow-lined quasars (i.e., with $\text{FWHM}(\text{H}\beta) \leq 2000 \text{ km s}^{-1}$) in the Baskin & Laor analysis. As already noted in this paper and by Vestergaard (2004), we agree that the C IV profiles in NLS1s are not suitable for the purpose of estimating virial masses on account of the probability that there is a strong component from an outflowing wind. We thus removed these objects from the sample.

A second problem is data screening, principally of the *IUE* spectra. The quality of *IUE* data on objects as faint as BQS quasars is low on account of the small aperture (0.45 m) of the *IUE* telescope and, by current standards, relatively insensitive detectors. In our opinion, only few of the *IUE* spectra of quasars are of adequate quality for mass estimates as we describe here. Also, some objects have relatively strong absorption superposed on the C IV profile, sometimes very close to line center. This makes it very challenging, or even impossible, to establish the intrinsic profile, especially at the spectral resolution of *IUE* and even for certain of the *HST* spectra (§ 2.2).

¹³Despite its many virtues, the BQS is limited in some applications because it is neither a complete sample nor representative of the typical quasar population. Compared with the SDSS sample, Jester et al. (2005) find that the BQS quasars tend to be bluer and brighter than typical quasars and that the BQS sample is incomplete at the 50% level. In addition, the PG sample of Boroson & Green contains a larger fraction of specific subgroups of objects such as NLS1s and narrow-lined quasars, as well as more powerful radio sources than typical quasar samples.

A final problem we identify is subtraction of a narrow-line component from the C IV profile. Narrow-component removal is important in the case of H β because it is a significant contributor to the total flux. It is also *possible* because the adjacent [O III] λ 5007 line can be used as a template profile. While Baskin & Laor are not the first to attempt to remove a narrow C IV component (cf. Bachev et al. 2004), there is little evidence that it is in fact necessary since the UV narrow-line components seem to be very weak (Wills et al. 1993). Moreover, it is not clear how to effect this since there are no isolated narrow lines in the UV to use as templates, so both the narrow line width and strength have to be guessed.

In addition to removing the 17 NLS1s from the sample, on the basis of inspection of the C IV line profiles shown in Fig. 1 of Baskin & Laor (2005), we have removed several additional spectra from the database because of insufficient quality, problematic narrow-component subtraction, or strong absorption. Omission of these objects and the 17 NLS1s and narrow-line quasars leaves us with 46 objects, which is 57% of the original sample. Our modified sample is listed in Table 6.

In Fig. 10, we show how our modified sample selection affects the parameter distributions presented by Baskin & Laor (2005). The full sample analyzed by Baskin & Laor is shown as open symbols, while the filled symbols denote the measurements which we consider to be more reliable, based entirely on Figure 1 and column (16) of Table 1 in their paper. The full (original) sample has a standard deviation (rms) of 0.22 dex around the unity line (hereafter, “case 1”) in the left panel of Fig. 10. Assuming that C IV is always emitted from a distance half that of H β as seen for NGC 5548 (Korista et al. 1995), the rms is 0.23 dex (hereafter, “case 2”). However, the significance of this is hard to judge since Baskin & Laor do not quote errors on their parameters. We examined to what extent the exclusion of the NLS1s and each additional subset (A: low quality *IUE* data; B: strong absorption; and C: subtraction of a strong ($\gtrsim 2\text{\AA}$) narrow C IV component) changes the rms in each case. The most significant changes are seen when the NLS1s alone are excluded. In this case, the rms reduces to 0.16 dex for case 1 and to 0.22 dex for case 2. When, in addition, the objects in subset C are also excluded, the rms reduces to 0.15 dex (case 1) and 0.21 dex (case 2), very similar to the rms of the modified sample (i.e., all data deemed to be unreliable are excluded; Table 6), namely 0.15 dex (case 1) and 0.22 dex (case 2). We conclude that for the modified sample, the FWHM(C IV) and FWHM(H β) values are correlated, albeit with some scatter (Fig 10, left panel).

For comparison, we examined the data in this work in a similar manner. Figure 11 (left panel) compares the single-epoch line widths of C IV and H β . Given the multiple FWHM entries for both C IV and H β , we choose to plot only the weighted means for each object of the FWHM(C IV) and FWHM(H β) values, respectively. The solid (red) error bars in the diagram represent the range in measured FWHM values based on the individual epoch FWHM measurements and the measurement errors. The best comparison is of line widths obtained at epochs in which a continuum change has had time to propagate to both the C IV and H β emitting regions. Since no statistically significant sample of such data exists, we are limited to comparing the single-epoch measurements regardless of observed epoch. This may introduce additional scatter. In order to check whether the results

based on single-epoch $H\beta$ line widths may be spurious, we also compare in Fig. 12 (left panel) the single-epoch C IV line widths versus the $H\beta$ FWHM values obtained at each epoch of the monitoring data studied by Peterson et al. (2004); the red error bars are larger in this figure because the $H\beta$ error bars represent the actual measurement errors rather than a lower-limit estimate of 10% as in the case of the single-epoch $H\beta$ measurements in Fig. 11. Figures 11 and 12 show that, as in the case of the modified BQS sample, the line widths of C IV and $H\beta$ are strongly correlated and that some, but not all, of the scatter can be attributed to measurement errors and the lack of simultaneity of the C IV and $H\beta$ measurements (red error bars); the rms values in these figures is similar to that of the the modified BQS sample (see captions).

There remains, however, an inverse correlation between the ratio of the C IV and $H\beta$ line widths and $\text{FWHM}(H\beta)$ in both samples, as seen in the right-hand panels in Figs. 10, 11, and 12. This could be attributable to a number of effects, including, for example, a small difference in the slopes of the $H\beta$ and C IV $R - L$ relationships. We defer discussion of this issue to a forthcoming paper, since for the present purposes, it is sufficient to note that differences in $H\beta$ and C IV line widths are now only of order ± 0.2 dex, or a factor 1.6. This translates to a difference in mass estimates of a factor 2.5, which is within the uncertainties of the single-epoch mass estimates.

Our reanalysis suggests that the mass estimates based on C IV may not be as untrustworthy as Baskin & Laor claim. Simply removing data points that are problematic for a number of reasons greatly reduces the discrepancies between C IV-based and $H\beta$ -based mass estimates. This is, of course, not to say that there are not systematic effects (which are the subject of several current investigations), but only that these effects are small relative to the level of accuracy to which we claim that we can measure the masses of AGN black holes at this time.

B. Mass Estimates for the PG Quasars

Table 7 lists the single-epoch mass estimates of the PG quasars studied by Boroson & Green (1992) without mass measurements from reverberation mapping techniques. The mass estimates are based on eq. (5) in the main text.

REFERENCES

- Akritas, M. G. & Bershadsky, M. A. 1996, *ApJ*, 470, 706
- Bachev, R., Marziani, P., Sulentic, J. W., Zamanov, R., Calvani, M., & Dultzin-Hacyan, D. 2004, *ApJ*, 617, 171
- Baskin, A., & Laor, A. 2005, *MNRAS*, 356, 1029
- Bentz, M. C., Peterson, B. M., Pogge, R. W., Vestergaard, M., & Onken, C. A. 2006, *ApJ*, submitted
- Boroson, T. A., & Green, R. F. 1992, *ApJS*, 80, 109

- Boroson, T. A. 2003, *ApJ*, 585, 647
- Cardelli, J. A., Clayton, G. C., Mathis, J. S., 1989, *ApJ*, 345, 245
- Clavel, J., et al., 1991, *ApJ*, 366, 64
- Crenshaw, D. M., Kraemer, S. B., Bruhweiler, F. C., & Ruiz, J. R. 2001, *ApJ*, 555, 633
- Collinge, M. J., et al. 2001, *ApJ*, 557, 2
- Dunlop, J. S. 2004, *Coevolution of Black Holes and Galaxies*, ed. L. C. Ho, (Pasadena: Carnegie Observatories), 342
- Ferrarese, L., Pogge, R. W., Peterson, B. M., Merritt, D., Wandel, A., & Joseph, C. L. 2001, *ApJ*, 555, L79
- Gaskell, C. M. 1982, *ApJ*, 263, 79
- Gebhardt, K., et al. 2000, *ApJ*, 543, L5
- Jester, S., et al. 2005, *AJ*, 130, 873
- Kaspi, S., Smith, P. S., Netzer, H., Maoz, D., Jannuzi, B. T., & Giveon, U. 2000, *ApJ*, 533, 631
- Kaspi, S., Maoz, D., Netzer, H., Peterson, B. M., Vestergaard, M., & Jannuzi, B. T. 2005, *ApJ*, 629, 61
- Kellermann, K. I., Sramek, R., Schmidt, M., Shaffer, D. B., & Green, R. 1989, *AJ*, 98, 1195
- Kollatschny, W. 2003, *A&A*, 407, 461
- Korista, K. T., et al. 1995, *ApJS*, 97, 285
- Laor, A. 2000, *ApJ*, 543, L111
- Leighly, K. M. 2000, *New Astronomy Review*, 44, 395
- Maoz, D. 2002, *astro-ph/0207295*
- Marziani, P., Sulentic, J. W., Dultzin-Hacyan, D., Calvani, M., & Moles, M. 1996, *ApJS*, 104, 37
- Marziani, P., Sulentic, J. W., Zamanov, R., Calvani, M., Dultzin-Hacyan, D., Bachev, R., & Zwitter, T. 2003, *ApJS*, 145, 199
- McLure, R.J., & Jarvis, M.J. 2002, *MNRAS*, 337, 109
- Miyoshi, M., Moran, J., Herrnstein, J., Greenhill, L., Nakai, N., Diamond, P., Inoue, M. 1995, *Nature*, 373, 127
- Nelson, C.H., Green, R.F., Bower, G., Gebhardt, K., & Weistrop, D. 2004, *ApJ*, 615, 652
- Neugebauer, G., Green, R. F., Matthews, K., Schmidt, M., Soifer, B. T., & Bennett, J. 1987, *ApJS*, 63, 615
- O’Brien, P. T., et al. 1998, *ApJ*, 509, 163
- Onken, C. A., Ferrarese, L., Merritt, D., Peterson, B. M., Pogge, R. W., Vestergaard, M., & Wandel, A. 2004, *ApJ*, 615, 645
- Onken, C.A., & Peterson, B.M. 2002, *ApJ*, 572, 746
- Peterson, B. M., & Wandel, A. 1999, *ApJ*, 521, L95
- Peterson, B. M., & Wandel, A. 2000, *ApJ*, 540, L13

- Peterson, B. M. et al. 2004, ApJ, 613, 682
- Peterson, B. M. et al. 2005, ApJ, 632, 799. Erratum in press.
- Press, W. H., Teukolsky, S. A., Vetterling, W. T., & Flannery, B. P. 1992, Numerical Recipes (2nd Ed.; Cambridge: University Press)
- Reichert, G.A., et al. (1994), ApJ, 425, 582
- Richards, G. T., Vanden Berk, D. E., Reichard, T. A., Hall, P. B., Schneider, D. P., SubbaRao, M., Thakar, A. R., & York, D. G. 2002, AJ, 124, 1
- Rodriguez-Pascual, P.M., et al. 1997, ApJS, 110, 9
- Schmidt, M., & Green, R. F. 1983, ApJ, 269, 352
- Schmidt, M., Schneider, D. P., & Gunn, J. E. 1995, AJ, 110, 68
- Shemmer, O., Netzer, H., Maiolino, R., Oliva, E., Croom, S., Corbett, E., & di Fabrizio, L. 2004, ApJ, 614, 547
- Tytler, D., & Fan, X. 1992, ApJS, 79, 1
- Vestergaard, M. 2002, ApJ, 571, 733 (Paper I)
- Vestergaard, M. 2004, ApJ, 601, 676
- Vestergaard, M., & Wilkes, B. J. 2001, ApJS, 134, 1
- Wandel, A., Peterson, B. M., & Malkan, M. A. 1999, ApJ, 526, 579
- Wanders, I., et al. 1997, ApJS, 113, 69
- Warner, C., Hamann, F., & Dietrich, M. 2003, ApJ, 596, 72
- Wilkes, B. J. 1984, MNRAS, 207, 73
- Wills, B. J., Netzer, H., Brotherton, M. S., Han, M., Wills, D., Baldwin, J. A., Ferland, G. J., & Browne, I. W. A. 1993, ApJ, 410, 534
- Wu, X.-B., Wang, R., Kong, M. Z., Liu, F. K., & Han, J. L. 2004, A&A, 424, 793

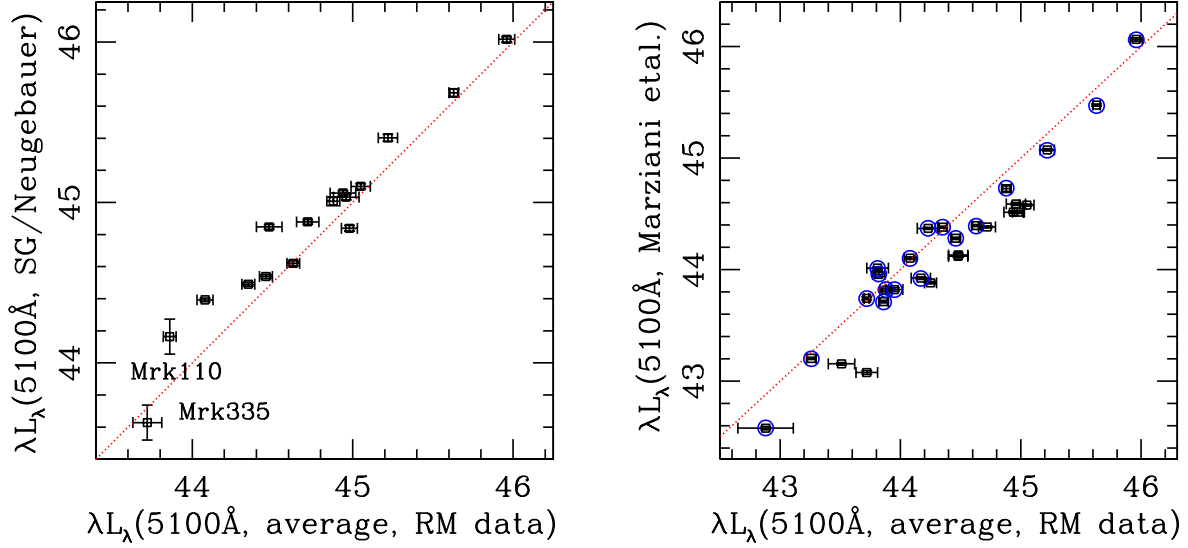


Fig. 1.— Comparison of the average $L_{\lambda}(5100\text{\AA})$ values determined from the monitoring data of Peterson et al. (2004) with the single-epoch 5100\AA continuum luminosities $L_{\lambda}(5100\text{\AA})$ based on (*Left*) Neugebauer et al. (1987) plus Schmidt & Green’s (1983) measurements of Mrk 110 and Mrk 335, and (*Right*) Marziani et al. (2003). The data points marked by (blue) circles in the right panel deviate less than 0.3 dex from the average monitoring luminosity. These data points are selected for calibration of eq. (1). The (red) dotted lines denote unity relationships.

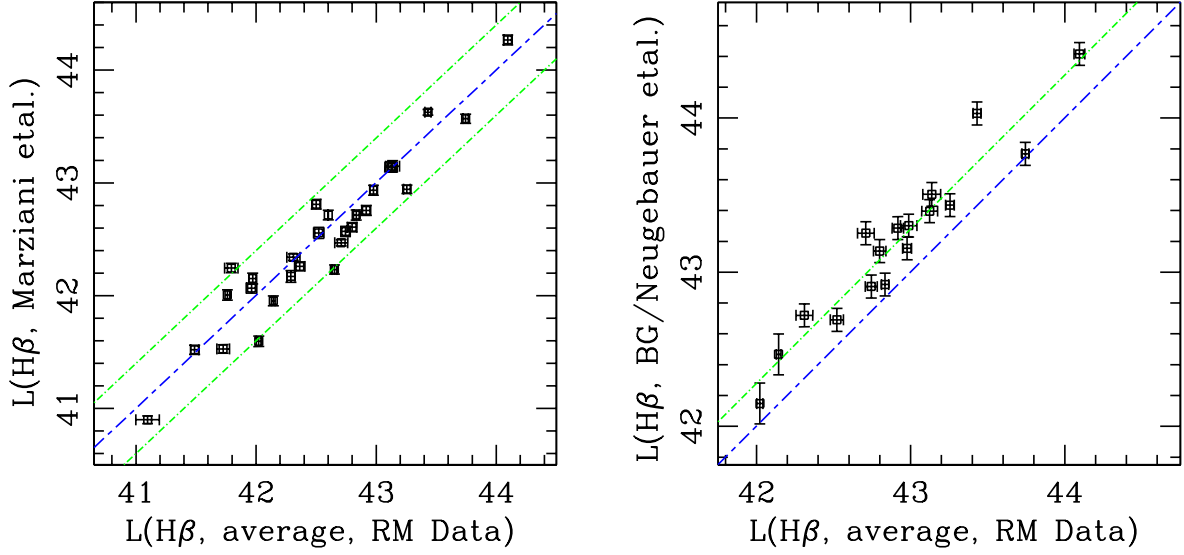


Fig. 2.— Comparison of the mean $H\beta$ line luminosities $L(H\beta)$ based on monitoring data with the single-epoch $L(H\beta)$ values determined based on (*left*) the Marziani et al. (2003) data, and (*right*) the combination of Boroson & Green (1992), Neugebauer et al. (1987), and Schmidt & Green (1992) data. (*Left*) The Marziani et al. line luminosities scatter well around a one-to-one relationship (blue short-long dashed line) and within approximately 0.4 dex as indicated by the (green) dot-dashed lines. The mean offset of the Marziani et al. measurements is -0.04 ± 0.21 dex. Combined with the even scatter around the monitoring values this indicates that the offsets are very likely to be due to variability (contrary to the Boroson & Green values; right panel). (*Right*) The line luminosities obtained based on the Boroson & Green and Neugebauer et al. measurements scatter evenly around a systematic offset of about 0.28 ± 0.15 dex (green dot-dashed line) from a one-to-one relationship (blue short-long dashed line). Origin of this systematic significant offset is unknown. Therefore, these data are not included in the analysis.

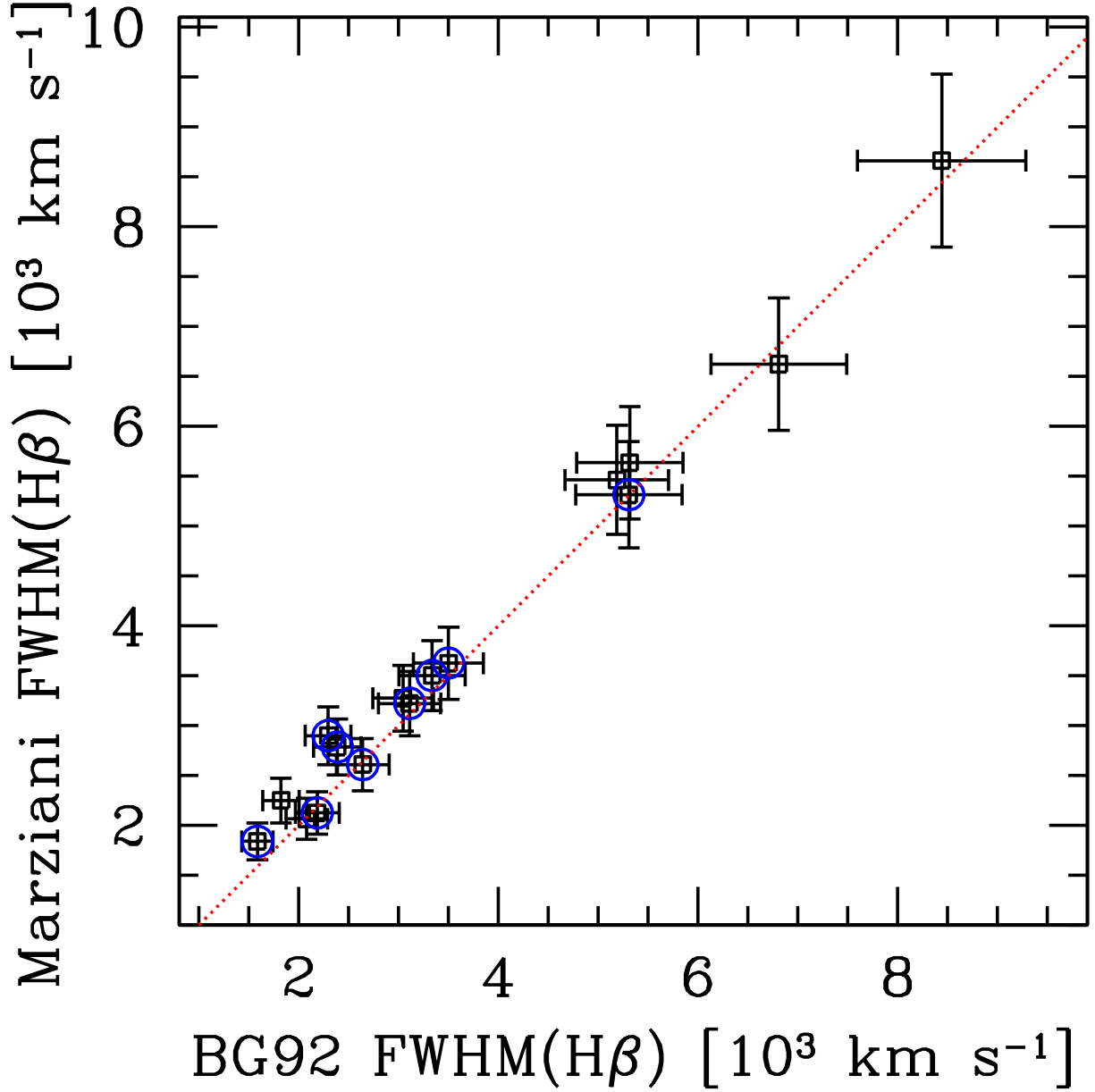


Fig. 3.— Comparison of the $\text{FWHM}(\text{H}\beta)$ measurements by Marziani et al. (2003) and Boroson & Green (1992) for the objects common to both studies. The dotted (red) line indicate a one-to-one relationship. The measurements are essentially consistent to within the (expected) errors. The data points marked by (blue) circles mark those objects for which the Marziani et al. 5100 Å continuum luminosity deviate by less than 0.3 dex from the average luminosity based on the monitoring data of Peterson et al. (2004). This shows that a more deviant continuum luminosity does not affect the line widths for the Marziani et al. sample.

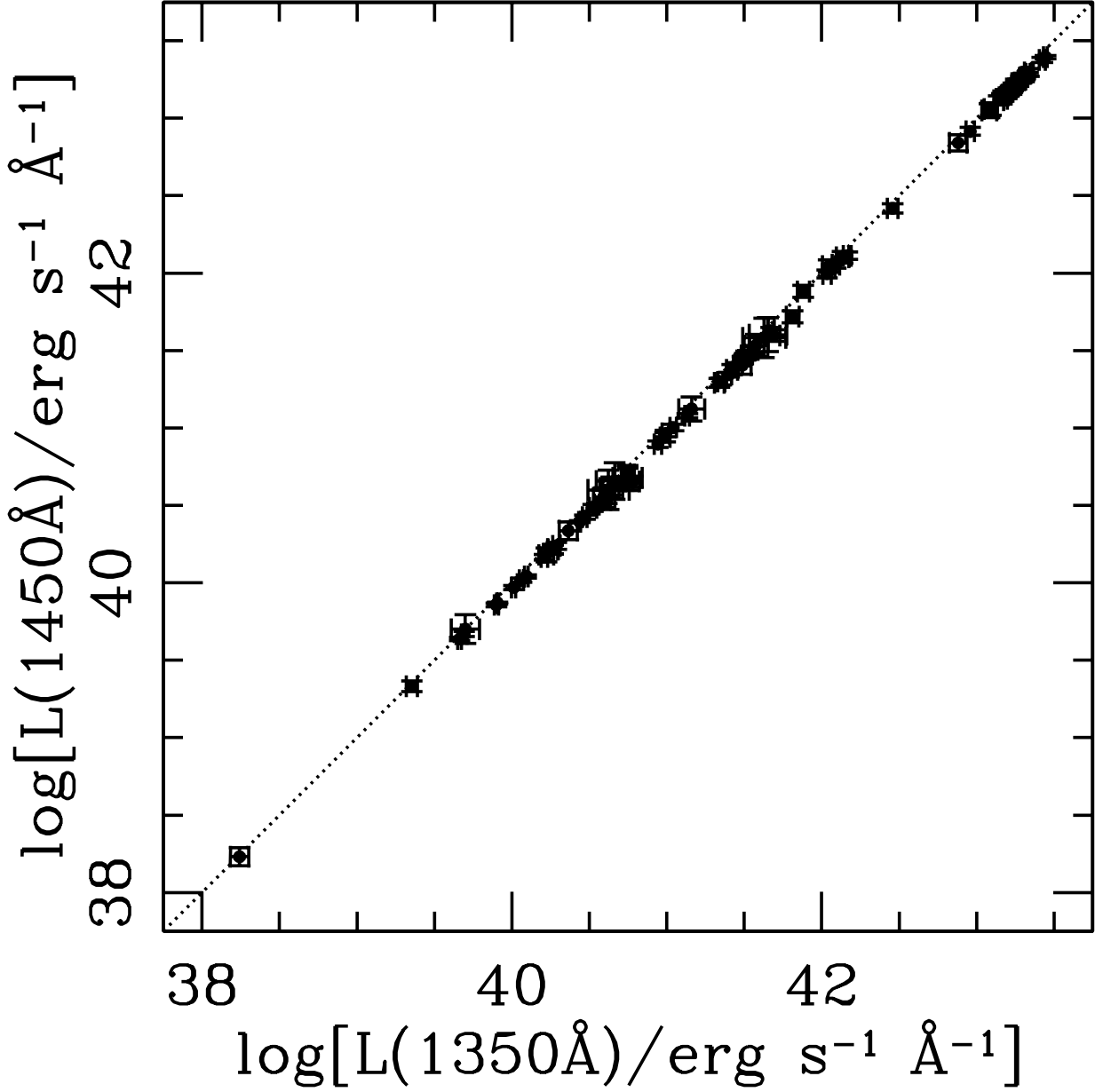


Fig. 4.— Comparison of the 1350Å and 1450Å continuum luminosities, $L_{\lambda}(1350)$ and $L_{\lambda}(1450)$ measured for the UV sample described in § 2.2. The two luminosities are so tightly correlated (scatter is within the measurement uncertainties) that separate scaling relationships for $L_{\lambda}(1450)$ are not needed. The two luminosity measures are interchangeable in the calibrated mass estimation (eqs. 5 and 6).

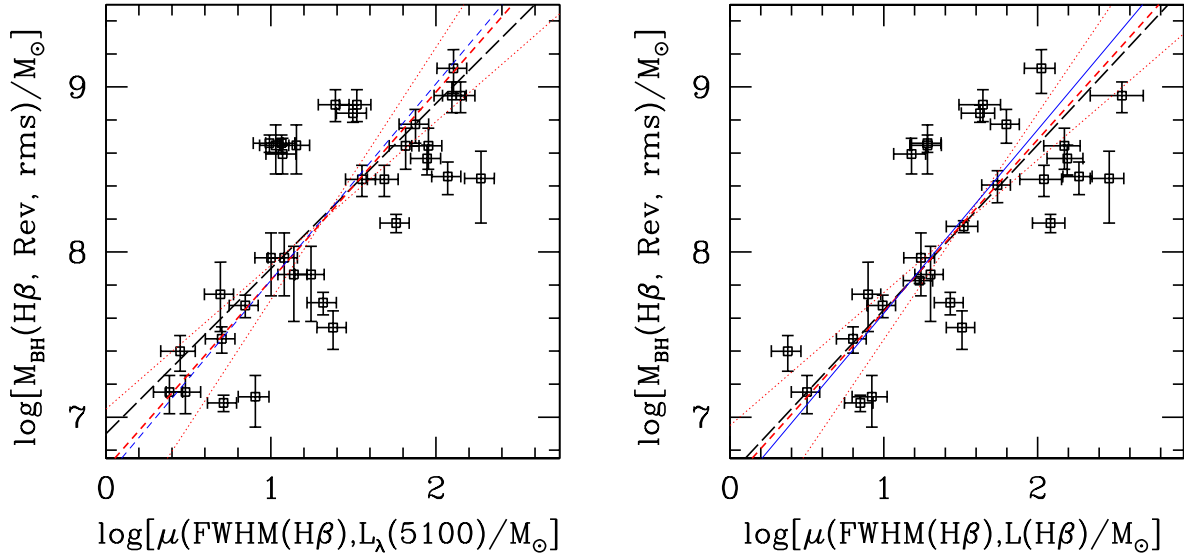


Fig. 5.— Distribution of normalized single-epoch unscaled mass estimates based on optical data with the reverberation mapping black hole masses. (*Left*) Unscaled mass estimates based on $\text{FWHM}(\text{H}\beta)$ and the continuum luminosity $L_{\lambda}(5100\text{\AA})$. (*Right*) Unscaled mass estimates based on $\text{FWHM}(\text{H}\beta)$ and the $\text{H}\beta$ line luminosity $L(\text{H}\beta)$. In both cases are the slopes consistent with unity (within the errors). *Symbols:* The (black) long-dashed line shows a slope of 1.0, the (red) short-dashed line denotes the BCES bisector, the (red) dotted lines show the BCES(Y|X) and BCES(X|Y) fits, and the (blue) short-long dashed line represent the FITEXY fit.

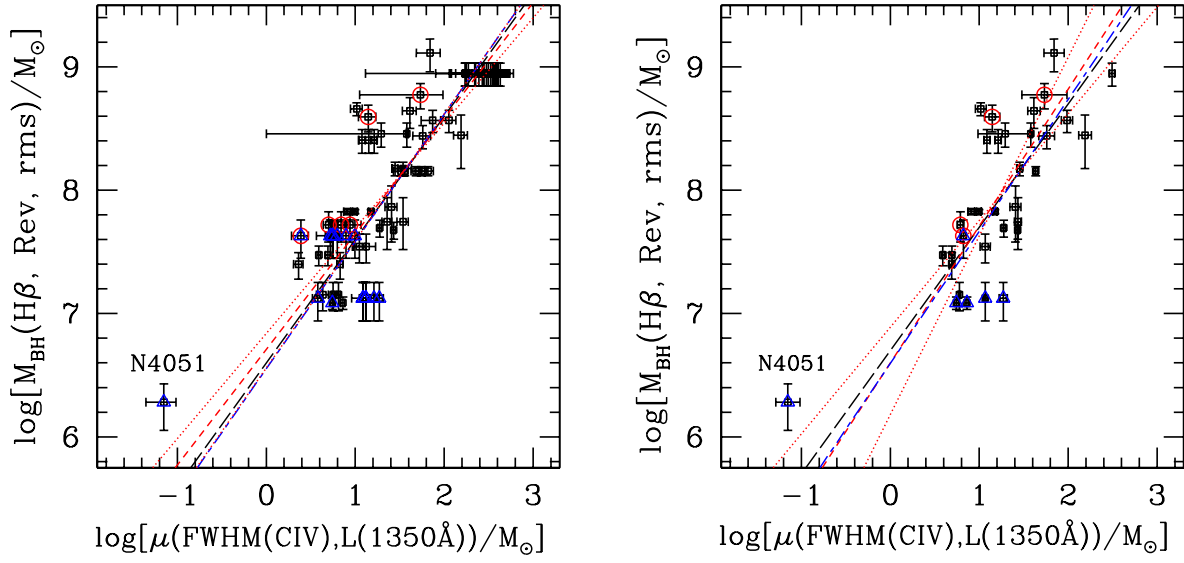


Fig. 6.— Distribution of normalized single-epoch unscaled mass estimates μ based on UV data, specifically the $\text{FWHM}(\text{C IV})$ and $L_{\lambda}(1350\text{\AA})$, with the reverberation mapping black hole masses: (*Left*) All individual measurements for each object in the sample; (*Right*) the weighted mean μ of individual (non-monitoring) measurements of a given object and the weighted mean of monitoring data when available. In both cases are the slopes consistent with unity (within the errors). *Symbols*: (red) encircled data points denote spectra flagged for being of borderline quality, and (blue) triangles mark spectra which were corrected for mild absorption in the C IV profile. See Fig. 5 for line codes.

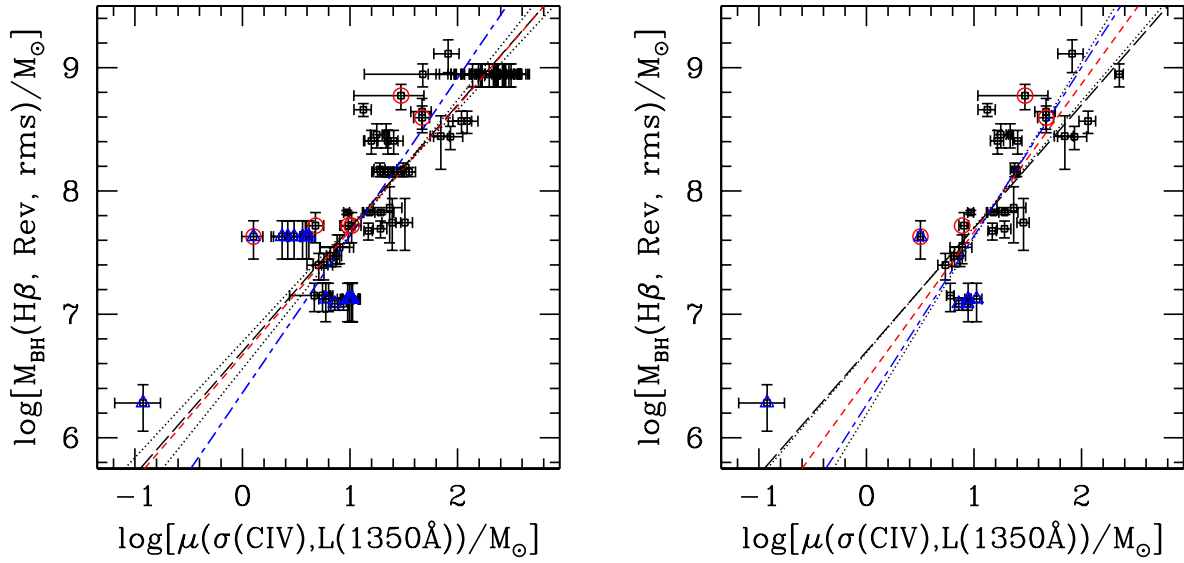


Fig. 7.— Distribution of single-epoch unscaled mass estimates μ based on UV data, specifically the line dispersion $\sigma_l(\text{CIV})$ and $L_{\lambda}(1350\text{\AA})$, with the reverberation mapping black hole masses: (*Left*) All individual measurements for each object in the sample; (*Right*) the weighted mean μ of individual (non-monitoring) measurements of a given object and the weighted mean of monitoring data when available. In both cases are the slopes consistent with unity (within the errors). For symbols, see Fig. 6.

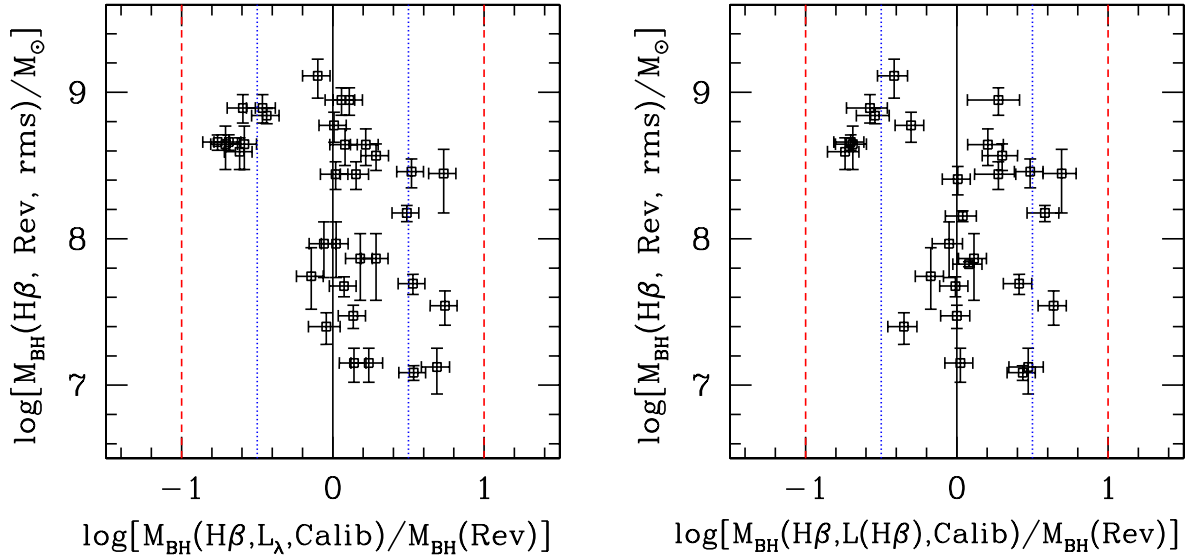


Fig. 8.— Deviation of the optical single-epoch black hole mass estimates from the reverberation mapping established mass $M_{\text{BH}}(\text{Rev})$ plotted versus $M_{\text{BH}}(\text{Rev})$. (*Left*) Single-epoch mass estimates based on FWHM($\text{H}\beta$) and $L_{\lambda}(5100\text{\AA})$. (*Right*) Single-epoch mass estimates based on FWHM($\text{H}\beta$) and $L(\text{H}\beta)$. The uncertainties in the abscissa are the (propagated) uncertainties in the single-epoch mass estimates (i.e., *not* the error in the mass deviation). A strictly unity relationship is indicated by the (black) solid line. Offsets of ± 0.5 dex and ± 1 dex are indicated by the (blue) dotted and (red) dashed lines, respectively.

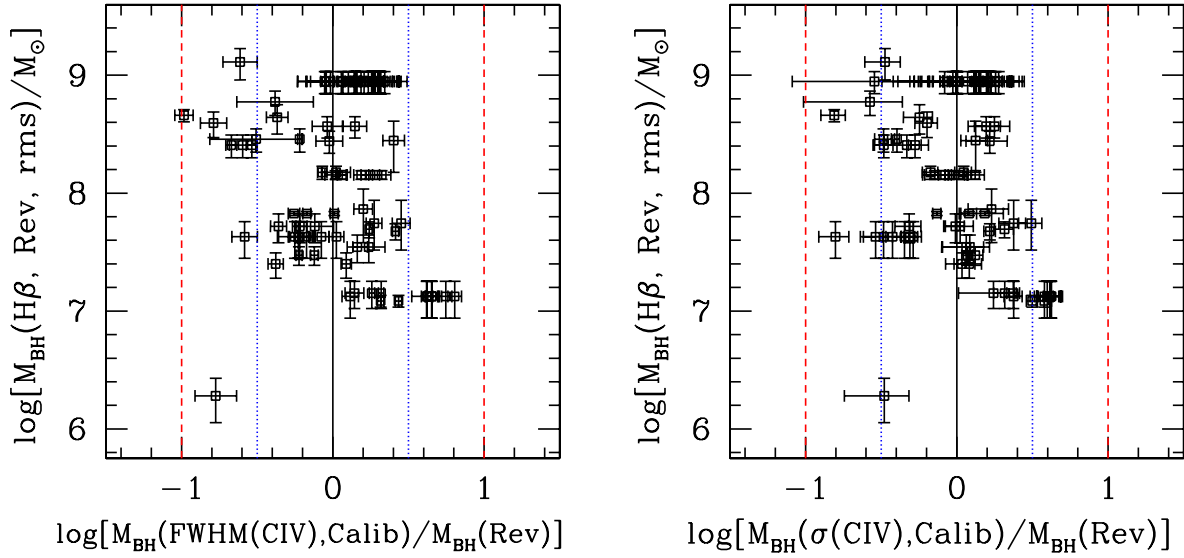


Fig. 9.— Deviation of the UV single-epoch black hole mass estimates from the reverberation mapping established mass $M_{\text{BH}}(\text{Rev})$ plotted versus $M_{\text{BH}}(\text{Rev})$. (*Left*) Single-epoch mass estimates based on $\text{FWHM}(\text{CIV})$ and $L_{\lambda}(1350\text{\AA})$. (*Right*) Single-epoch mass estimates based on the line dispersion $\sigma_l(\text{CIV})$ and $L_{\lambda}(1350\text{\AA})$. The uncertainties in the abscissa are the (propagated) uncertainties in the single-epoch mass estimates (i.e., *not* the error in the mass deviation). A strictly unity relationship is indicated by the (black) solid line. Offsets of ± 0.5 dex and ± 1 dex are indicated by the (blue) dotted and (red) dashed lines, respectively.

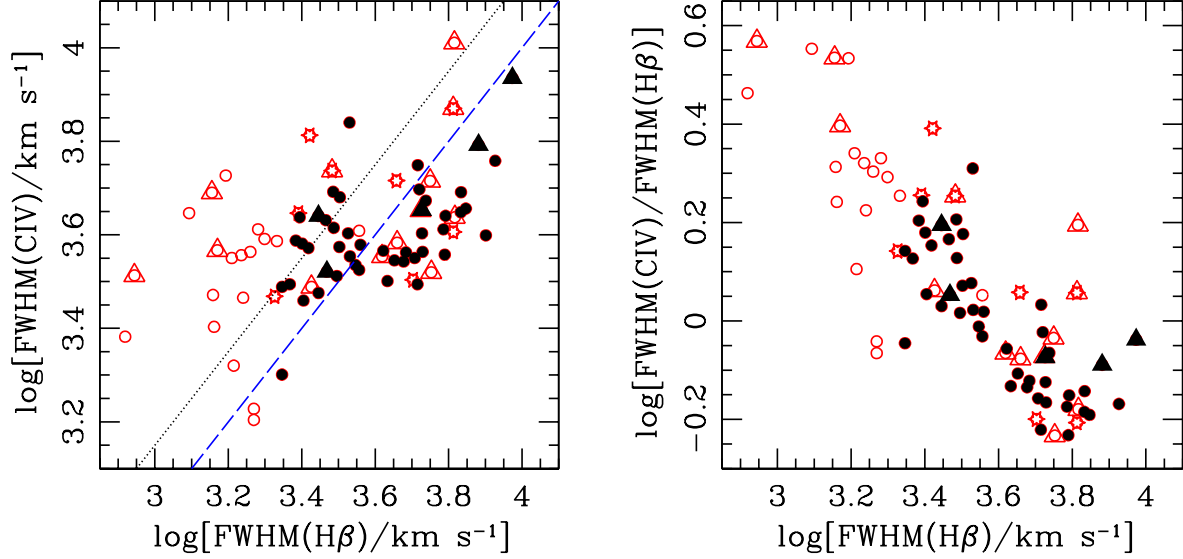


Fig. 10.— Relationship between the C IV and H β line widths for the BQS sample. (*Left*) The FWHM(C IV) and FWHM(H β) are compared directly. The unity relationship (blue dashed line) is shown for comparison. The (black) dotted line shows the expected relationship if FWHM(C IV) is always $\sqrt{2}$ larger than FWHM(H β). (*Right*) The ratio of line widths are compared to FWHM(H β). Symbols: The original sample analyzed by Baskin & Laor (2005) is shown with (red) open symbols. The objects for which a NLR contribution stronger than 2\AA is subtracted from the C IV profile are marked by open (red) stars. Entries that are based on bad profile fits owing to low quality *IUE* data or bad absorption are marked with open (red) triangles superposed on the (red) open circle. The modified and reanalyzed sample (see text) is shown with filled symbols. Entries among those with borderline quality *IUE* data or C IV profile absorption are marked with solid triangles. In the left diagram, the rms around the (blue) dashed line for the original sample is 0.22 dex and 0.15 dex for the modified sample.

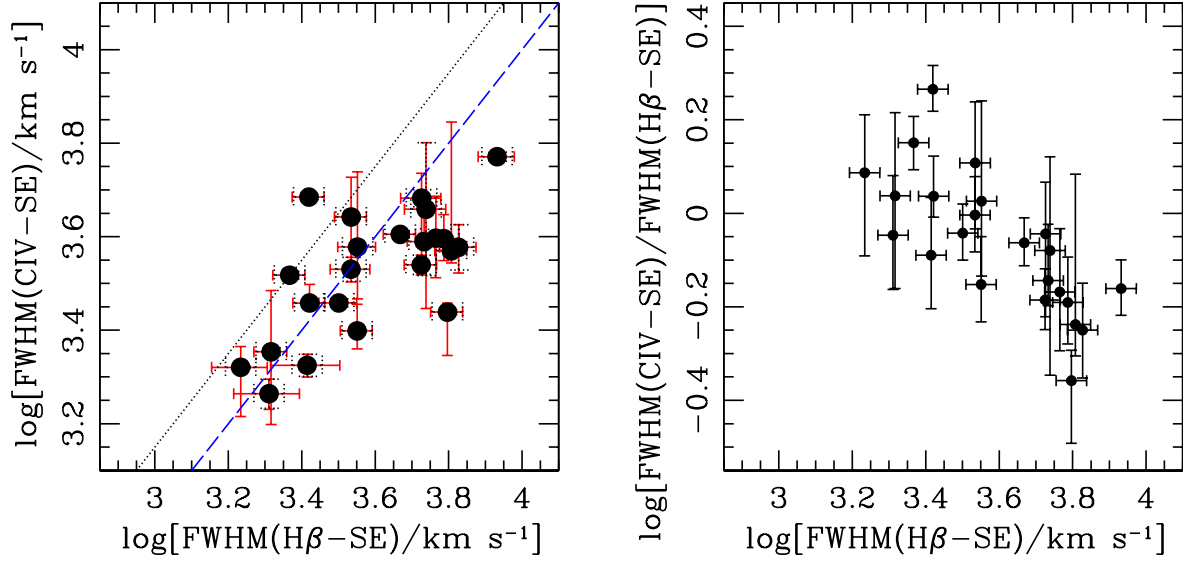


Fig. 11.— Relationship between the single-epoch C IV and single-epoch H β line widths for the UV reverberation sample. The data points are the weighted average of each FWHM entry in Tables 1 and 2. (*Left*) The FWHM(C IV) and FWHM(H β) are compared directly. The unity relationship (blue dashed line) is shown for comparison. The (black) dotted line shows the expected relationship if FWHM(C IV) is always $\sqrt{2}$ larger than FWHM(H β). The black dotted error bars are the errors on the weighted means, while the (red) solid error bars show the range of line widths covered by the individual measurements and their errors. The rms of the data points around the unity relation is 0.23 dex and relative to the black dotted relationship is 0.33 dex; the average “error bar” is 0.06 dex and 13% of the errors exceed 0.1 dex up to a maximum value of 0.41 dex. (*Right*) The ratio of line widths are compared to FWHM(H β). The error bar for the ratio is based on the available ranges of linewidths and measurement errors (red/solid error bars in the left diagram).

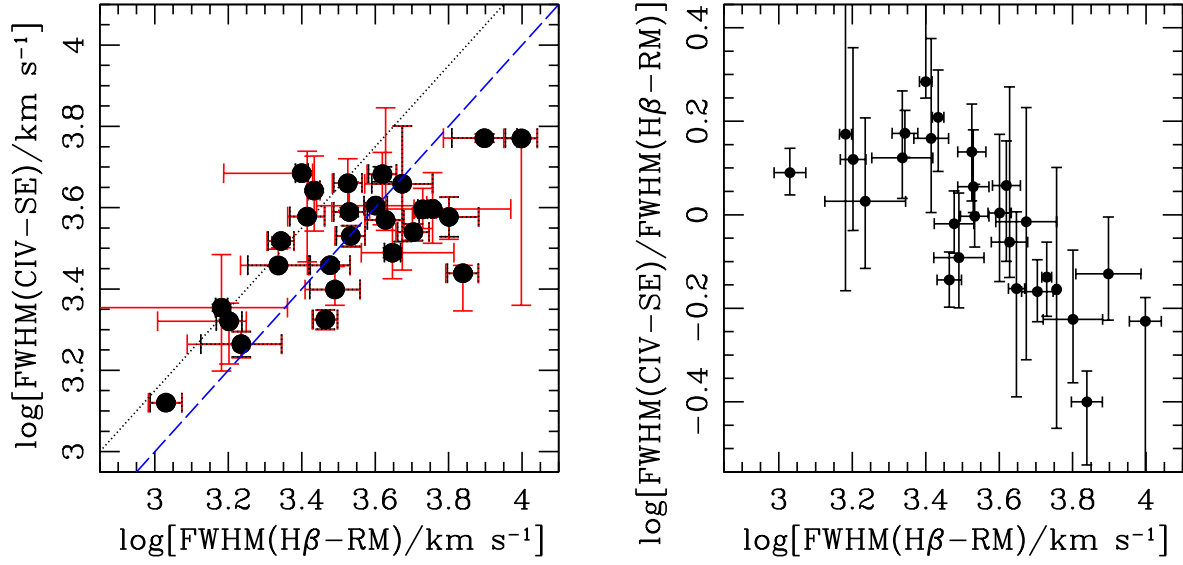


Fig. 12.— Relationship between the single-epoch C IV and H β line widths for the current sample. The H β data are the weighted average of the FWHM of the individual epoch spectra listed by Peterson et al. (2004). The C IV data points are likewise the weighted average of each FWHM entry in Table 2. (*Left*) The FWHM(C IV) and FWHM(H β) are compared directly. The rms of the data points around the unity relation is 0.16 dex and relative to the black dotted relationship is 0.23 dex; the average “error bar” is 0.07 dex and 33% of the errors exceed 0.1 dex up to a maximum value of 0.41 dex. (*Right*) The ratio of line widths are compared to FWHM(H β). See Figure 11 for symbols.

Table 1. Optical Spectral Parameters and Masses

Object	Alternative Name	z^a	FWHM($H\beta$) ^b (km s ⁻¹)	Ref.	$\log [\lambda L_\lambda (5100\text{\AA})$ /ergs s ⁻¹]	$\log [L(H\beta)$ /ergs s ⁻¹]	Ref.	$\log [M/M_\odot]^c$ ($H\beta, L_\lambda, SE$)	$\log [M/M_\odot]^c$ ($H\beta, L(H\beta), SE$)	$\log [M/M_\odot]^d$ ($H\beta, rms$)
(1)	(2)	(3)	(4)	(5)	(6)	(7)	(8)	(9)	(10)	(11)
Mrk335	PG0003+199	0.02578	1585	1	44.16±0.118	...	4	7.379 ^{+0.099} _{-0.129}	...	7.152 ^{+0.101} _{-0.131}
			1841	2	43.71±0.011	41.95±0.043	2	7.192 ^{+0.081} _{-0.099}	7.175 ^{+0.083} _{-0.102}	
PG0026+129		0.14200	1821	1	45.10±0.017	...	3	8.059 ^{+0.098} _{-0.126}	...	8.594 ^{+0.095} _{-0.122}
			2250	2	...	42.76±0.043	2	...	7.855 ^{+0.091} _{-0.116}	
PG0052+251		0.15500	5187	1	45.03±0.017	...	3	8.926 ^{+0.096} _{-0.123}	...	8.567 ^{+0.081} _{-0.100}
			5463	2	...	43.14±0.044	2	...	8.867 ^{+0.101} _{-0.132}	
Fairall9		0.04702	6261	2	...	42.23±0.041	2	...	8.413 ^{+0.083} _{-0.103}	8.407 ^{+0.086} _{-0.108}
Mrk590		0.02638	2627	2	44.01±0.009	42.24±0.041	2	7.690 ^{+0.079} _{-0.097}	7.667 ^{+0.083} _{-0.103}	7.677 ^{+0.063} _{-0.074}
3C120		0.03301	2328	2	43.92±0.011	42.26±0.039	2	7.529 ^{+0.080} _{-0.097}	7.572 ^{+0.083} _{-0.103}	7.744 ^{+0.195} _{-0.226}
Akn120		0.03230	6120	2	44.37±0.007	42.81±0.042	2	8.652 ^{+0.082} _{-0.101}	8.758 ^{+0.092} _{-0.118}	8.176 ^{+0.052} _{-0.059}
PG0804+761		0.10000	3045	1	45.06±0.014	...	3	8.479 ^{+0.096} _{-0.124}	...	8.841 ^{+0.049} _{-0.055}
			3276	2	...	42.94±0.037	2	...	8.299 ^{+0.095} _{-0.120}	
PG0844+349	TON951	0.06400	2386	1	44.49±0.012	...	3	7.909 ^{+0.083} _{-0.103}	...	7.966 ^{+0.150} _{-0.231}
			2787	2	44.38±0.010	42.56±0.050	2	7.975 ^{+0.082} _{-0.101}	7.915 ^{+0.089} _{-0.111}	
Mrk110	PG0921+525	0.03529	2079	1	43.63± 0.11	...	4	7.276 ^{+0.100} _{-0.130}	...	7.400 ^{+0.094} _{-0.121}
			2067	2	...	41.6±0.0465	2	...	7.050 ^{+0.086} _{-0.107}	
PG0953+414	K348-7	0.23410	3111	1	45.40±0.022	...	3	8.715 ^{+0.107} _{-0.143}	...	8.441 ^{+0.084} _{-0.104}
			3224	2	45.07±0.011	43.63±0.026	2	8.536 ^{+0.097} _{-0.125}	8.715 ^{+0.115} _{-0.157}	
NGC3783		0.00973	3555	2	43.20±0.010	41.52±0.041	2	7.443 ^{+0.090} _{-0.113}	7.474 ^{+0.086} _{-0.107}	7.474 ^{+0.072} _{-0.087}
NGC4151		0.00332	6421	2	42.58±0.016	40.90±0.034	2	7.566 ^{+0.108} _{-0.143}	7.596 ^{+0.099} _{-0.128}	7.124 ^{+0.129} _{-0.184}
PG1226+023	3C273	0.15830	3500	1	46.02±0.017	...	3	9.204 ^{+0.128} _{-0.183}	...	8.947 ^{+0.083} _{-0.103}
			3627	2	46.06±0.014	44.27±0.043	2	9.262 ^{+0.130} _{-0.186}	9.222 ^{+0.139} _{-0.206}	
PG1229+204	TON1542	0.06301	3335	1	44.39±0.012	...	3	8.139 ^{+0.082} _{-0.101}	...	7.865 ^{+0.171} _{-0.285}
			3504	2	44.10±0.012	42.34±0.029	2	7.997 ^{+0.080} _{-0.098}	7.978 ^{+0.083} _{-0.102}	
PG1307+085		0.15500	5307	1	45.01±0.028	...	3	8.930 ^{+0.096} _{-0.123}	...	8.643 ^{+0.107} _{-0.142}
			5315	2	44.73±0.024	43.15±0.050	2	8.756 ^{+0.089} _{-0.111}	8.848 ^{+0.102} _{-0.134}	
Mrk279		0.03045	5411	2	43.82±0.017	42.07±0.045	2	8.198 ^{+0.080} _{-0.099}	8.183 ^{+0.083} _{-0.103}	7.543 ^{+0.102} _{-0.133}
PG1411+442	PB1732	0.08960	2640	1	44.62±0.014	...	3	8.080 ^{+0.086} _{-0.107}	...	8.646 ^{+0.124} _{-0.174}
			2611	2	44.39±0.010	42.72±0.045	2	7.924 ^{+0.082} _{-0.101}	7.958 ^{+0.091} _{-0.115}	
NGC5548		0.01717	5822	2	...	41.53±0.038	2	...	7.907 ^{+0.085} _{-0.107}	7.827 ^{+0.017} _{-0.017}
PG1426+015	Mrk1383	0.08647	6808	1	44.88±0.014	...	3	9.065 ^{+0.092} _{-0.116}	...	9.113 ^{+0.113} _{-0.153}
			6624	2	...	42.61±0.041	2	...	8.699 ^{+0.088} _{-0.111}	
Mrk817		0.03145	4657	2	43.96±0.022	42.15±0.048	2	8.156 ^{+0.080} _{-0.098}	8.106 ^{+0.084} _{-0.104}	7.694 ^{+0.063} _{-0.074}
PG1613+658	Mrk876	0.12900	8441	1	44.84±0.018	...	3	9.226 ^{+0.091} _{-0.115}	...	8.446 ^{+0.165} _{-0.270}
			8662	2	...	42.94±0.044	2	...	9.139 ^{+0.096} _{-0.123}	
PG1617+175	Mrk877	0.11240	5316	1	44.85±0.014	...	3	8.830 ^{+0.091} _{-0.115}	...	8.774 ^{+0.091} _{-0.115}
			5636	2	...	42.47±0.027	2	...	8.471 ^{+0.084} _{-0.105}	

Table 1—Continued

Object	Alternative Name	z^a	FWHM($H\beta$) ^b (km s ⁻¹)	Ref. (5)	$\log [\lambda L_\lambda(5100\text{\AA})$ /ergs s ⁻¹]	$\log [L(H\beta)$ /ergs s ⁻¹]	Ref. (8)	$\log [M/M_\odot]^c$ ($H\beta, L_\lambda, \text{SE}$)	$\log [M/M_\odot]^c$ ($H\beta, L(H\beta), \text{SE}$)	$\log [M/M_\odot]^d$ ($H\beta, \text{rms}$)
(1)	(2)	(3)	(4)		(6)	(7)		(9)	(10)	(11)
PG1700+518		0.29200	2185	1	45.68±0.025	...	3	8.585 ^{+0.117} _{-0.160}	...	8.893 ^{+0.091} _{-0.103}
			2127	2	45.47±0.010	43.57±0.041	2	8.427 ^{+0.109} _{-0.146}	8.319 ^{+0.114} _{-0.156}	
3C390.3		0.05610	40000	2	43.82±0.017	42.17±0.052	2	8.893 ^{+0.080} _{-0.099}	8.943 ^{+0.085} _{-0.105}	8.458 ^{+0.087} _{-0.110}
Mrk509		0.03440	3424	2	...	42.72±0.042	2	...	8.194 ^{+0.090} _{-0.114}	8.155 ^{+0.035} _{-0.038}
PG2130+099	II Zw 136	0.06298	2294	1	44.54±0.012	...	3	7.906 ^{+0.084} _{-0.104}	...	8.660 ^{+0.049} _{-0.056}
			2901	2	44.28±0.011	42.57±0.045	2	7.947 ^{+0.081} _{-0.099}	7.958 ^{+0.088} _{-0.111}	
NGC7469		0.01632	2639	2	43.74±0.012	42.01±0.045	2	7.524 ^{+0.081} _{-0.099}	7.521 ^{+0.083} _{-0.103}	7.086 ^{+0.047} _{-0.053}

^aRedshifts are obtained from the NASA/IPAC Extragalactic Database.

^bFWHM($H\beta$) measured in the single-epoch spectrum in units of km s⁻¹.

^cThe central mass (and uncertainties) estimated based on single-epoch optical spectroscopy.

^dThe central mass (and uncertainties) determined from multi-epoch spectrophotometry and reverberation mapping techniques. All values are adopted from Peterson et al. (2004).

References. — (1) Boroson & Green 1992; (2) Marziani et al. 2003; (3) Neugebauer et al. 1987; (4) Schmidt, & Green 1983; Kellerman, et al. 1989; Schmidt, Schneider, & Gunn (1995)

Table 2. Ultraviolet Spectral Parameters and Masses

Object (1)	Date Observed (2)	z (3)	Telescope/ Instrument (4)	Resolution (Å) (5)	FWHM(CIV) ^a (km s ⁻¹) (6)	σ (CIV) ^b (km s ⁻¹) (7)	$\log[\lambda L_{\lambda}/\text{erg s}^{-1}]$ (1350Å) (8)	$\log[M/M_{\odot}]^c$ (FWHM(CIV),SE) (9)	$\log[M/M_{\odot}]^c$ (σ (CIV),SE) (10)	Note (11)
Mrk 335	1989/10/29 – – 1991/06/30	0.02578	<i>IUE</i> /SWP	6.0	2291± 27	2116± 160	44.173±0.020	7.471 ^{+0.018} _{-0.018}	7.469 ^{+0.062} _{-0.073}	
	1990/10/12		<i>HUT</i>	3.0	1741± 99	1806± 360	44.291±0.078	7.295 ^{+0.062} _{-0.073}	7.394 ^{+0.150} _{-0.231}	
	1994/12/16		<i>HST</i> /FOS	1.4	2023± 17	2140± 93	44.262±0.013	7.410 ^{+0.018} _{-0.019}	7.526 ^{+0.040} _{-0.044}	
PG 0026+129	1994/11/27	0.14200	<i>HST</i> /FOS	1.4	1837± 136	3364± 70	45.165±0.025	7.805 ^{+0.087} _{-0.108}	8.397 ^{+0.068} _{-0.080}	flg
PG 0052+251	1992/06/29	0.15500	<i>IUE</i> /SWP	6.0	3983± 370	5118± 486	45.265±0.037	8.530 ^{+0.100} _{-0.130}	8.815 ^{+0.101} _{-0.132}	
	1993/07/22		<i>HST</i> /FOS	2.2	5192± 251	5083± 437	45.176±0.041	8.713 ^{+0.078} _{-0.095}	8.761 ^{+0.094} _{-0.120}	
Fairall 9	1993/01/22	0.04702	<i>HST</i> /FOS	2.2	2593± 65	2981± 197	44.470±0.028	7.736 ^{+0.037} _{-0.040}	7.924 ^{+0.061} _{-0.071}	
	1994/04/28 –12/26		<i>IUE</i> /SWP ^d	6.0	2831± 40	3532± 92	44.582±0.011	7.871 ^{+0.036} _{-0.039}	8.131 ^{+0.040} _{-0.044}	ref(1)
	1995/03/11		<i>HUT</i>	3.0	2370± 151	2978± 508	44.759±0.126	7.811 ^{+0.088} _{-0.111}	8.076 ^{+0.143} _{-0.214}	
Mrk 590	1991/01/14	0.02638	<i>IUE</i> /SWP	6.0	4839± 59	3574± 141	44.119±0.029	8.091 ^{+0.020} _{-0.020}	7.895 ^{+0.037} _{-0.040}	
3C 120	1993/08/25	0.03301	<i>IUE</i> /SWP	6.0	3302± 75	3199± 169	44.943±0.039	8.196 ^{+0.059} _{-0.068}	8.236 ^{+0.070} _{-0.083}	
	1994/02/19,27;03/11		<i>IUE</i> /SWP	6.0	3278± 105	3409± 286	44.617±0.056	8.017 ^{+0.052} _{-0.059}	8.119 ^{+0.079} _{-0.097}	
Akn 120	1988/01/20;02/12; 1991/01/13	0.03230	<i>IUE</i> /SWP	6.0	3989± 451	3795± 165	44.634±0.021	8.197 ^{+0.095} _{-0.121}	8.221 ^{+0.052} _{-0.059}	
	1995/07/29		<i>HST</i> /FOS	1.4	3945± 42	3240± 149	44.482±0.022	8.106 ^{+0.031} _{-0.034}	8.002 ^{+0.048} _{-0.054}	
Mrk 79	1978/04/15	0.02219	<i>IUE</i> /SWP	6.0	3182± 521	3344± 222	43.879±0.039	7.600 ^{+0.124} _{-0.175}	7.710 ^{+0.058} _{-0.067}	flg
	1979/11/14		<i>IUE</i> /SWP	6.0	3049± 128	2971± 248	43.495±0.058	7.360 ^{+0.053} _{-0.060}	7.404 ^{+0.077} _{-0.094}	flg
	1982/12/28		<i>IUE</i> /SWP	6.0	3113± 122	3803± 388	43.726±0.065	7.500 ^{+0.048} _{-0.054}	7.741 ^{+0.087} _{-0.109}	flg
Mrk 110	1988/02/28	0.03529	<i>IUE</i> /SWP	6.0	2990± 64	2601± 272	43.770±0.050	7.488 ^{+0.034} _{-0.037}	7.434 ^{+0.086} _{-0.108}	
	1988/02/29		<i>IUE</i> /SWP	6.0	1638± 59	2576± 231	43.876±0.081	7.022 ^{+0.051} _{-0.057}	7.482 ^{+0.081} _{-0.100}	
PG 0953+414	1991/06/17; 1992/11/04–05	0.23410	<i>HST</i> /FOS	1.5	2873± 57	3512± 361	45.588±0.031	8.418 ^{+0.089} _{-0.111}	8.659 ^{+0.115} _{-0.157}	
NGC 3516	1995/03/12	0.00884	<i>HUT</i>	2.0	4675± 538	3311± 372	42.830±0.093	7.379 ^{+0.115} _{-0.157}	7.146 ^{+0.114} _{-0.154}	abs
	1995/12/30		<i>HST</i> /FOS	1.4	4875± 17	3132± 64	42.823±0.017	7.411 ^{+0.066} _{-0.078}	7.094 ^{+0.068} _{-0.080}	abs
	1996/02/21		<i>HST</i> /FOS	1.4	5147± 103	3245± 84	43.192±0.013	7.654 ^{+0.049} _{-0.055}	7.320 ^{+0.051} _{-0.058}	abs
	1996/04/13		<i>HST</i> /FOS	1.4	4729± 28	3430± 92	43.143±0.013	7.554 ^{+0.049} _{-0.056}	7.342 ^{+0.053} _{-0.061}	abs
	1996/08/14		<i>HST</i> /FOS	1.4	4525± 97	3137± 79	43.030±0.012	7.456 ^{+0.057} _{-0.066}	7.205 ^{+0.058} _{-0.067}	abs
	1996/11/28		<i>HST</i> /FOS	1.4	3940± 18	2834± 95	42.485±0.034	7.047 ^{+0.084} _{-0.104}	6.828 ^{+0.088} _{-0.110}	abs,flg
	1998/04/13		<i>HST</i> /STIS/G140L	0.88	4912± 23	3973± 36	42.793±0.012	7.402 ^{+0.067} _{-0.080}	7.284 ^{+0.068} _{-0.080}	abs
NGC 3783	1991/12/21 – – 1992/07/29	0.00973	<i>IUE</i> /SWP ^d	6.0	2831± 22	3273± 100	43.601±0.014	7.352 ^{+0.025} _{-0.027}	7.545 ^{+0.035} _{-0.038}	ref(2)
	1992/07/27	0.00973	<i>HST</i> /FOS	1.95	2308± 17	3179± 185	43.744±0.022	7.250 ^{+0.020} _{-0.021}	7.595 ^{+0.051} _{-0.058}	
NGC 4051	2000/03/25	0.00234	<i>HST</i> /STIS/E140M	0.13	1319± 13	1713± 227	41.373±0.058	5.507 ^{+0.137} _{-0.201}	5.801 ^{+0.163} _{-0.263}	abs,ref(3)
NGC 4151	1993/11/27 –12/15	0.00332	<i>IUE</i> /SWP ^d	6.0	6929± 76	5220± 123	43.224±0.010	7.929 ^{+0.045} _{-0.051}	7.750 ^{+0.048} _{-0.054}	abs,ref(5)
	1995/03/04–05		<i>HUT</i>	2.0	5418± 150	4604± 249	43.340±0.019	7.777 ^{+0.045} _{-0.050}	7.703 ^{+0.058} _{-0.067}	
	1995/03/07		<i>HUT</i>	2.0	5062± 51	4651± 371	43.396±0.029	7.747 ^{+0.039} _{-0.042}	7.741 ^{+0.073} _{-0.088}	abs
	1995/03/10		<i>HUT</i>	2.0	5246± 44	4675± 397	43.396±0.031	7.778 ^{+0.039} _{-0.043}	7.745 ^{+0.077} _{-0.093}	abs
	1995/03/13		<i>HUT</i>	2.0	5752± 144	4585± 321	43.418±0.023	7.870 ^{+0.041} _{-0.045}	7.740 ^{+0.066} _{-0.078}	abs
	1995/03/15		<i>HUT</i>	2.0	5173± 593	4664± 475	43.354±0.044	7.744 ^{+0.098} _{-0.126}	7.721 ^{+0.090} _{-0.113}	abs
	1998/02/10,06/01		<i>HST</i> /STIS/G140L	0.88	3509± 10	4384± 66	43.038±0.006	7.239 ^{+0.054} _{-0.062}	7.500 ^{+0.056} _{-0.064}	abs,ref(4)
3C 273	1991/01/14,15,17	0.15834	<i>HST</i> /FOS	1.5	3941± 266	4027± 322	46.336±0.008	9.088 ^{+0.130} _{-0.187}	9.174 ^{+0.134} _{-0.194}	
	1991/01/23;06/17		<i>IUE</i> /SWP	6.0	3673± 420	3604± 954	46.467±0.026	9.097 ^{+0.150} _{-0.230}	9.147 ^{+0.212} _{-0.432}	
	1991/07/09		<i>HST</i> /FOS	2.2	3693± 843	3495± 501	46.089±0.026	8.901 ^{+0.188} _{-0.338}	8.920 ^{+0.149} _{-0.228}	
	1991/12/07,12		<i>IUE</i> /SWP	6.0	3834± 155	3425± 556	46.309±0.018	9.050 ^{+0.124} _{-0.174}	9.019 ^{+0.163} _{-0.264}	
	1992/01/05		<i>IUE</i> /SWP	6.0	3645± 447	3098± 811	46.323±0.026	9.014 ^{+0.148} _{-0.226}	8.940 ^{+0.208} _{-0.414}	

Table 2—Continued

Object (1)	Date Observed (2)	z (3)	Telescope/ Instrument (4)	Resolution (Å) (5)	FWHM(CIV) ^a (km s ⁻¹) (6)	σ (CIV) ^b (km s ⁻¹) (7)	$\log[\lambda L_{\lambda}/\text{erg s}^{-1}]$ (1350Å) (8)	$\log[M/M_{\odot}]^c$ (FWHM(CIV),SE) (9)	$\log[M/M_{\odot}]^c$ (σ (CIV),SE) (10)	Note (11)
3C 273	1992/01/18;02/01,15	0.15834	<i>IUE</i> /SWP	6.0	4671± 127	3597± 560	46.377±0.015	9.258 ^{+0.125} _{-0.176}	9.098 ^{+0.162} _{-0.262}	
	1992/05/06;06/05		<i>IUE</i> /SWP	6.0	4349± 420	3643± 762	46.555±0.017	9.290 ^{+0.147} _{-0.224}	9.203 ^{+0.190} _{-0.345}	
	1992/06/05,21;07/05		<i>IUE</i> /SWP	6.0	4167± 178	3685± 434	46.575±0.011	9.263 ^{+0.135} _{-0.198}	9.224 ^{+0.154} _{-0.242}	
	1992/12/17,28,29		<i>IUE</i> /SWP	6.0	3784± 219	3445± 706	46.437±0.020	9.107 ^{+0.133} _{-0.192}	9.092 ^{+0.185} _{-0.329}	
	1992/12/31		<i>IUE</i> /SWP	6.0	4715± 764	3669± 633	46.274±0.029	9.211 ^{+0.162} _{-0.262}	9.060 ^{+0.167} _{-0.274}	
	1993/01/02		<i>IUE</i> /SWP	6.0	4354±1952	3442± 725	46.012±0.052	9.003 ^{+0.288} _{-1.228}	8.866 ^{+0.179} _{-0.309}	
	1993/01/03		<i>IUE</i> /SWP	6.0	3434± 238	1785± 574	46.213±0.045	8.903 ^{+0.127} _{-0.180}	8.402 ^{+0.234} _{-0.543}	
	1993/01/04–06,09		<i>IUE</i> /SWP	6.0	4554± 131	2953± 517	46.425±0.015	9.261 ^{+0.127} _{-0.181}	8.952 ^{+0.172} _{-0.288}	
	1993/01/16		<i>IUE</i> /SWP	6.0	3950± 884	3714± 801	46.336±0.027	9.091 ^{+0.191} _{-0.350}	9.104 ^{+0.187} _{-0.337}	
	1993/02/01a		<i>IUE</i> /SWP	6.0	4454± 629	3740± 491	46.398±0.021	9.227 ^{+0.157} _{-0.249}	9.143 ^{+0.153} _{-0.239}	
	1993/02/01b		<i>IUE</i> /SWP	6.0	3128± 198	3398± 423	46.419±0.018	8.932 ^{+0.133} _{-0.193}	9.071 ^{+0.151} _{-0.235}	
	1993/02/13;05/12,27; 1993/12/14,27;									
	1994/01/08,14,24		<i>IUE</i> /SWP	6.0	4599± 163	3580± 394	46.395±0.015	9.253 ^{+0.127} _{-0.180}	9.103 ^{+0.145} _{-0.220}	
	1994/01/24;02/07,23		<i>IUE</i> /SWP	6.0	4098± 143	3793± 568	46.396±0.020	9.154 ^{+0.127} _{-0.180}	9.154 ^{+0.160} _{-0.257}	
	1994/02/07,23		<i>IUE</i> /SWP	6.0	4617± 145	3776± 943	46.292±0.033	9.203 ^{+0.122} _{-0.171}	9.095 ^{+0.202} _{-0.390}	
	1994/05/03,15		<i>IUE</i> /SWP	6.0	4426± 337	3685± 438	46.444±0.015	9.246 ^{+0.137} _{-0.201}	9.154 ^{+0.150} _{-0.232}	
	1994/05/15		<i>IUE</i> /SWP	6.0	3058± 41	3015± 519	46.382±0.023	8.893 ^{+0.124} _{-0.175}	8.947 ^{+0.169} _{-0.281}	
	1994/05/30;06/15,20,27		<i>IUE</i> /SWP	6.0	4278± 80	3697± 358	46.461±0.012	9.226 ^{+0.128} _{-0.182}	9.166 ^{+0.143} _{-0.216}	
	1994/12/30		<i>IUE</i> /SWP	6.0	4567± 134	3795± 688	46.387±0.025	9.243 ^{+0.126} _{-0.178}	9.149 ^{+0.174} _{-0.293}	
	1995/01/03,05–07,09; 1995/01/12,29;02/14		<i>IUE</i> /SWP	6.0	4344± 116	3730± 313	46.411±0.013	9.213 ^{+0.126} _{-0.179}	9.147 ^{+0.138} _{-0.203}	
	1995/05/03,17,18,31; 1995/06/14,27		<i>IUE</i> /SWP	6.0	4387± 95	3532± 350	46.337±0.014	9.182 ^{+0.123} _{-0.171}	9.061 ^{+0.140} _{-0.207}	
	1995/12/21,26,31; 1996/01/05,10,16,18,20; 1996/01/22,24,26,28,30		<i>IUE</i> /SWP	6.0	4430± 237	3503± 614	46.380±0.018	9.213 ^{+0.129} _{-0.185}	9.076 ^{+0.171} _{-0.285}	
	1996/01/20		<i>IUE</i> /SWP	6.0	4452± 641	3314± 998	46.222±0.040	9.134 ^{+0.153} _{-0.239}	8.944 ^{+0.225} _{-0.492}	
PG 1229+204	1982/05,1983/06	0.06301	<i>IUE</i> /SWP	6.0	3391± 205	3241± 457	44.654±0.028	8.066 ^{+0.062} _{-0.073}	8.094 ^{+0.113} _{-0.154}	
PG 1307+085	1993/07/21	0.15500	<i>HST</i> /FOS	2.2	3465± 168	3687± 290	45.012±0.039	8.275 ^{+0.071} _{-0.085}	8.396 ^{+0.085} _{-0.106}	
Mrk 279	1995/03/05	0.03045	<i>HUT</i>	2.0	4126± 487	3118± 414	43.795±0.118	7.781 ^{+0.106} _{-0.141}	7.605 ^{+0.115} _{-0.157}	
	1995/03/11		<i>HUT</i>	2.0	3876± 99	3286± 511	43.754±0.127	7.705 ^{+0.067} _{-0.079}	7.629 ^{+0.130} _{-0.186}	
NGC 5548	1988/12/14 – – 1989/08/07	0.01717	<i>IUE</i> /SWP ^d	6.0	4790± 67	4815± 257	43.654±0.022	7.836 ^{+0.026} _{-0.028}	7.908 ^{+0.049} _{-0.055}	ref(6)
	1993/04/19 –05/27		<i>HST</i> /FOS ^d	1.9	4096± 14	3973± 34	43.568±0.006	7.655 ^{+0.026} _{-0.027}	7.695 ^{+0.026} _{-0.028}	ref(7)
	1995/03/14		<i>HUT</i>	2.0	3280± 27	5050± 787	43.773±0.069	7.570 ^{+0.038} _{-0.042}	8.012 ^{+0.122} _{-0.170}	
PG 1426+015	1985/03/01–02	0.08647	<i>IUE</i> /SWP	6.0	3778± 448	4101± 391	45.295±0.023	8.500 ^{+0.113} _{-0.154}	8.638 ^{+0.101} _{-0.133}	
Mrk 817	1981/11/06,07; 1982/07/18		<i>IUE</i> /SWP	6.0	4027± 71	4062± 289	44.123±0.022	7.934 ^{+0.020} _{-0.021}	8.009 ^{+0.059} _{-0.068}	
PG 1613+658	1990/12/02,05,08,10; 1991/02/25		<i>IUE</i> /SWP	6.0	5902± 136	3965± 215	45.221±0.023	8.848 ^{+0.071} _{-0.083}	8.570 ^{+0.080} _{-0.098}	
PG 1617+175	1993/05/13	0.11244	<i>IUE</i> /SWP	6.0	4558±1763	3383±1036	44.784±0.108	8.392 ^{+0.253} _{-0.683}	8.200 ^{+0.214} _{-0.439}	flg
3C 390	1994/12/31 – – 1996/03/05	0.05610	<i>IUE</i> /SWP ^d	6.0	5895± 32	4454± 53	44.073±0.022	8.239 ^{+0.013} _{-0.013}	8.062 ^{+0.016} _{-0.016}	ref(8)
	1996/03/31		<i>HST</i> /FOS	1.4	4676±2386	4444± 263	43.909±0.035	7.951 ^{+0.306} _{-7.951}	7.973 ^{+0.052} _{-0.059}	

Table 2—Continued

Object (1)	Date Observed (2)	z (3)	Telescope/ Instrument (4)	Resolution (Å) (5)	FWHM(CIV) ^a (km s ⁻¹) (6)	σ (CIV) ^b (km s ⁻¹) (7)	$\log [\lambda L_{\lambda}/\text{erg s}^{-1}]$ (1350Å) (8)	$\log [M/M_{\odot}]^c$ (FWHM(CIV),SE) (9)	$\log [M/M_{\odot}]^c$ (σ (CIV),SE) (10)	Note (11)
Mrk 509	1992/02/22	0.03440	<i>IUE</i> /SWP	6.0	5035± 298	3558± 205	44.641±0.029	8.403 ^{+0.061} _{-0.072}	8.168 ^{+0.061} _{-0.070}	
	1992/06/21		<i>HST</i> /FOS	2.0	4345± 49	3426± 115	44.532±0.015	8.217 ^{+0.033} _{-0.036}	8.078 ^{+0.042} _{-0.046}	
	1992/10/25,26,29		<i>IUE</i> /SWP	6.0	4973± 233	3647± 172	44.803±0.020	8.478 ^{+0.060} _{-0.069}	8.276 ^{+0.060} _{-0.069}	
	1993/10/27; 1993/11/09		<i>IUE</i> /SWP	6.0	4961± 218	3127± 226	44.552±0.033	8.343 ^{+0.050} _{-0.057}	8.009 ^{+0.068} _{-0.080}	
	1995/03/16		<i>HUT</i>	2.0	3716± 228	3174± 448	44.706±0.071	8.173 ^{+0.071} _{-0.086}	8.104 ^{+0.118} _{-0.162}	
PG 2130+099	1995/07/24	0.06298	<i>HST</i> /GHRS	0.65	2113± 119	2390± 184	44.692±0.025	7.676 ^{+0.061} _{-0.071}	7.850 ^{+0.073} _{-0.088}	
NGC 7469	1996/06/10 – – 07/29	0.01632	<i>IUE</i> /SWP ^d	6.0	3094± 53	3379± 182	43.774±0.016	7.520 ^{+0.021} _{-0.022}	7.664 ^{+0.047} _{-0.052}	ref(9)
	1996/06/18		<i>HST</i> /FOS	1.4	2860± 12	3266± 110	43.679±0.015	7.402 ^{+0.021} _{-0.022}	7.584 ^{+0.035} _{-0.038}	abs

^aSpectral resolution corrected line width FWHM(CIV) measured in the single-epoch spectrum in units of km s⁻¹.

^bSpectral resolution corrected line dispersion σ (CIV) measured in the single-epoch spectrum in units of km s⁻¹.

^cThe central mass (and uncertainties; see text), listed in logarithmic units, estimated based on the single-epoch UV spectroscopic measurements and the calibrations (equations 3 and 4) described in the text.

^dThis spectrum is the average of the data obtained during an AGN Watch monitoring campaign. An average spectrum was used to avoid cluttering the data base.

Note. — abs — Absorption in CIV profile is interpolated across; flg — flagged objects. See main text (§ 2.2.3) for details.

References. — (1) Rodriguez-Pascual et al. 1997; (2) Reichert et al. 1994; (3) Collinge et al. 2001; (4) Crenshaw et al. 2001 (5) Crenshaw et al. 1996; (6) Clavel, et al. 1991; (7) Korista, et al. 1995; (8) O’Brien, et al. 1998; (9) Wanders, et al. 1997.

Table 3. Regression Results

Unscaled Mass Estimate (1)	N (2)	BCES Fit		FITEXY Fit			Note (8)
		Slope (3)	Intercept (4)	Slope (5)	Intercept (6)	Scatter ^a (7)	
$\mu[\text{FWHM}(\text{H}\beta), \text{L}(5100\text{\AA})]$	34	1.14 ± 0.11	6.69 ± 0.15	1.19 ± 0.19	6.64 ± 0.24	51%	
$\mu[\text{FWHM}(\text{H}\beta), \text{L}(\text{H}\beta)]$	28	1.04 ± 0.13	6.60 ± 0.18	1.11 ± 0.21	6.52 ± 0.28	50%	
$\mu[\text{FWHM}(\text{CIV}), \text{L}(1350\text{\AA})]$	85	0.94 ± 0.05	6.71 ± 0.10	1.03 ± 0.07	6.55 ± 0.10	42%	
	84	0.97 ± 0.05	6.65 ± 0.10	1.06 ± 0.08	6.52 ± 0.10	42%	1
	34	1.11 ± 0.18	6.60 ± 0.25	1.19 ± 0.17	6.47 ± 0.20	52%	2
	33	1.29 ± 0.16	6.35 ± 0.21	1.32 ± 0.23	6.31 ± 0.26	51%	1,2
$\mu[\sigma(\text{CIV}), \text{L}(1350\text{\AA})]$	85	1.01 ± 0.06	6.67 ± 0.11	1.28 ± 0.10	6.37 ± 0.13	34%	
	84	1.04 ± 0.06	6.62 ± 0.11	1.33 ± 0.11	6.30 ± 0.12	33%	1
	34	1.21 ± 0.19	6.47 ± 0.26	1.37 ± 0.16	6.27 ± 0.20	42%	2
	33	1.41 ± 0.17	6.19 ± 0.22	1.52 ± 0.20	6.08 ± 0.25	40%	1,2

^aGiven in percent of the measurement value, μ and M_{BH} (Rev); symmetric in dependent and independent variable.

Note. — 1 – Object NGC 4051 is excluded. 2 – Weighted means. There are 34 entries because of the 27 objects five have each an additional average entry and NGC 5548 has two additional average entries that are based on average monitoring data that are not included in the weighted means; see §3.3 for details.

Note. — BCES results are those obtained from the bootstrapping pertaining to the bisector as they are considered less sensitive toward outliers (a few thousand realizations are made in each fitting); the bootstrapping method tends to yield larger errors and sometimes steeper slopes than the formal BCES results, owing mostly to the position of the NGC 4051 data point. See text for details. For each UV unscaled mass μ in column 1 four rows are given: the first two rows are the results of fitting all the multiple data sets for each object (including and excluding NGC 4051, see column 8), and the next two rows are the results where all data sets per object (excluding measurements based on mean monitoring spectra) were averaged, again excluding NGC 4051 in the second row as noted in column 8.

Table 4. Mass Scaling Relationships — Zeropoints

Unscaled Mass Estimate (1)	N (2)	Average Zeropoint (dex) (3)	Std. Dev. (dex) (4)	Note (5)
$\mu[\text{FWHM}(\text{H}\beta), \text{L}(5100\text{\AA})]$	34	6.907 ± 0.024	0.43	
$\mu[\text{FWHM}(\text{H}\beta), \text{L}(\text{H}\beta)]$	28	6.674 ± 0.026	0.43	
$\mu[\text{FWHM}(\text{CIV}), \text{L}(1350\text{\AA})]$	85	6.659 ± 0.011	0.36	
	34	6.691 ± 0.012	0.43	Weighted mean
$\mu[\sigma(\text{CIV}), \text{L}(1350\text{\AA})]$	85	6.726 ± 0.013	0.33	
	34	6.726 ± 0.015	0.37	Weighted mean

Note. — For each UV unscaled mass μ in column 1 two rows are given: first row is the fit results where multiple data sets were used for each object, and the second row is the fit results where all data sets per object (excluding measurements based on mean monitoring spectra) were averaged. See text for details.

Table 5. Probabilities of Mass Estimate Accuracies

Calibration (1)	Relative Accuracy					Absolute Accuracy Estimate ^a (7)
	Factor of 3 (0.5 dex) (2)	Factor of 6 (0.78 dex) (3)	Factor of 10 (1.0 dex) (4)	1 σ (68%) (5)	2 σ (95%) (6)	
FWHM(H β), L(5100Å)	22/34 \approx 65%	34/34 = 100%	34/34 = 100%	0.52 dex	0.73 dex	0.70 dex
FWHM(H β), L(H β)	20/28 \approx 70%	28/28 = 100%	28/28 = 100%	0.47 dex	0.70 dex	0.66 dex
FWHM(CIV), L(1350Å)	70/85 \approx 82%	82/85 \approx 96%	85/85 = 100%	0.32 dex	0.67 dex	0.56 dex
σ (CIV), L(1350Å)	73/85 \approx 86%	83/85 \approx 98%	85/85 = 100%	0.32 dex	0.62 dex	0.56 dex

^aThe estimated upper limit in the absolute accuracy of the reverberation mapping masses of a factor 2.9 (see text) is included here to provide an estimate of the absolute statistical uncertainty of the single-epoch mass estimates.

Table 6. Modified Bright Quasar Survey Sample^a

Objects				
0003+158	0007+106	0049+171	0052+251	0804+761
0838+770 ^b	0844+349	0923+201 ^b	0947+396	0953+414
1049−006	1100+772	1103−006	1116+215	1121+422
1149−110	1151+117	1216+069	1226+023	1229+204
1259+593	1302−102	1307+085	1309+355	1310−108
1322+659	1352+183	1415+451	1416−129	1425+267 ^b
1426+015	1427+480	1435−067	1444+407	1501+106
1512+370	1519+226	1534+580	1545+210	1612+261
1613+658	1617+175 ^b	1626+554	2112+059	2130+099
2308+098				

^aThis is the modified sample of PG quasars, revisited in Appendix A, which is considered to have more robust restframe UV spectral measurements.

^bBorderline *IUE* quality data or borderline absorption in *C IV* profile. These object entries are flagged in Figure 10.

Table 7. Mass Estimates of Boroson & Green PG Quasar Sample

Object	z	FWHM(H β) ^a (km s ⁻¹)	log [λL_{λ} ^b /ergs s ⁻¹]	log [M/M_{\odot}] ^c (H β , L_{λ} , SE)
(1)	(2)	(3)	(4)	(5)
PG 0003+158	0.45000	4750.7	46.018 ^{+0.033} _{-0.036}	9.270 ^{+0.088} _{-0.110}
PG 0007+106	0.08900	5084.6	44.816 ^{+0.014} _{-0.015}	8.728 ^{+0.081} _{-0.099}
PG 0043+039	0.38400	5290.8	45.537 ^{+0.030} _{-0.032}	9.123 ^{+0.085} _{-0.105}
PG 0049+171	0.06400	5234.3	44.004 ^{+0.011} _{-0.011}	8.347 ^{+0.079} _{-0.097}
PG 0050+124	0.06100	1171.4	44.794 ^{+0.097} _{-0.126}	7.441 ^{+0.093} _{-0.119}
PG 0157+001	0.16400	2431.9	44.975 ^{+0.017} _{-0.018}	8.166 ^{+0.081} _{-0.100}
PG 0838+770	0.13100	2763.8	44.727 ^{+0.015} _{-0.015}	8.154 ^{+0.080} _{-0.099}
PG 0923+129	0.02900	7598.4	43.860 ^{+0.097} _{-0.125}	8.598 ^{+0.092} _{-0.117}
PG 0923+201	0.19000	1956.7	45.038 ^{+0.018} _{-0.019}	8.009 ^{+0.082} _{-0.101}
PG 0934+013	0.05000	1254.3	43.875 ^{+0.097} _{-0.126}	7.041 ^{+0.092} _{-0.117}
PG 0947+396	0.20600	4816.7	44.808 ^{+0.020} _{-0.021}	8.677 ^{+0.081} _{-0.100}
PG 1001+054	0.16100	1699.8	44.741 ^{+0.017} _{-0.017}	7.738 ^{+0.081} _{-0.099}
PG 1004+130	0.24000	6290.4	45.536 ^{+0.022} _{-0.023}	9.272 ^{+0.084} _{-0.104}
PG 1011-040	0.05800	1381.0	44.259 ^{+0.012} _{-0.012}	7.317 ^{+0.079} _{-0.097}
PG 1012+008	0.18500	2614.7	45.011 ^{+0.021} _{-0.022}	8.247 ^{+0.082} _{-0.101}
PG 1022+519	0.04500	1566.4	43.696 ^{+0.097} _{-0.126}	7.145 ^{+0.092} _{-0.117}
PG 1048-090	0.34400	5610.8	45.596 ^{+0.027} _{-0.029}	9.203 ^{+0.085} _{-0.105}
PG 1048+342	0.16700	3580.9	44.708 ^{+0.018} _{-0.019}	8.369 ^{+0.081} _{-0.099}
PG 1049-005	0.35700	5350.6	45.633 ^{+0.028} _{-0.030}	9.180 ^{+0.085} _{-0.106}
PG 1100+772	0.31300	6151.2	45.575 ^{+0.026} _{-0.027}	9.272 ^{+0.085} _{-0.105}
PG 1103-006	0.42500	6182.6	45.667 ^{+0.033} _{-0.036}	9.323 ^{+0.086} _{-0.107}
PG 1114+445	0.14400	4554.4	44.734 ^{+0.017} _{-0.017}	8.591 ^{+0.081} _{-0.099}
PG 1115+407	0.15400	1678.8	44.619 ^{+0.017} _{-0.018}	7.667 ^{+0.080} _{-0.099}
PG 1116+215	0.17700	2896.9	45.397 ^{+0.018} _{-0.019}	8.529 ^{+0.083} _{-0.103}
PG 1119+120	0.04900	1772.9	44.132 ^{+0.012} _{-0.012}	7.470 ^{+0.079} _{-0.097}
PG 1121+422	0.23400	2192.3	44.883 ^{+0.022} _{-0.023}	8.030 ^{+0.081} _{-0.100}
PG 1126-041	0.06000	2111.1	44.385 ^{+0.012} _{-0.012}	7.749 ^{+0.080} _{-0.098}
PG 1149-110	0.04900	3032.2	44.107 ^{+0.097} _{-0.126}	7.924 ^{+0.092} _{-0.117}
PG 1151+117	0.17600	4284.3	44.756 ^{+0.020} _{-0.021}	8.549 ^{+0.081} _{-0.099}
PG 1202+281	0.16500	5036.4	44.601 ^{+0.027} _{-0.029}	8.612 ^{+0.081} _{-0.099}
PG 1211+143	0.08500	1816.9	45.071 ^{+0.014} _{-0.014}	7.961 ^{+0.082} _{-0.101}
PG 1216+069	0.33400	5179.9	45.721 ^{+0.027} _{-0.028}	9.196 ^{+0.085} _{-0.106}
PG 1244+026	0.04800	720.6	43.801 ^{+0.030} _{-0.032}	6.523 ^{+0.080} _{-0.099}
PG 1259+593	0.47200	3377.3	45.906 ^{+0.034} _{-0.037}	8.917 ^{+0.087} _{-0.109}
PG 1302-102	0.28600	3383.4	45.827 ^{+0.024} _{-0.026}	8.879 ^{+0.086} _{-0.107}
PG 1309+355	0.18400	2917.3	45.014 ^{+0.019} _{-0.020}	8.344 ^{+0.082} _{-0.100}
PG 1310-108	0.03500	3606.0	43.725 ^{+0.010} _{-0.011}	7.884 ^{+0.079} _{-0.097}
PG 1322+659	0.16800	2765.4	44.980 ^{+0.098} _{-0.126}	8.281 ^{+0.094} _{-0.120}
PG 1341+258	0.08700	3013.9	44.344 ^{+0.097} _{-0.126}	8.037 ^{+0.092} _{-0.117}
PG 1351+236	0.05500	6527.2	44.048 ^{+0.011} _{-0.011}	8.560 ^{+0.079} _{-0.097}
PG 1351+640	0.08700	5646.1	44.835 ^{+0.014} _{-0.015}	8.828 ^{+0.081} _{-0.099}
PG 1352+183	0.15800	3580.6	44.816 ^{+0.017} _{-0.017}	8.423 ^{+0.081} _{-0.099}
PG 1354+213	0.30000	4126.7	44.977 ^{+0.072} _{-0.086}	8.627 ^{+0.088} _{-0.110}

Table 7—Continued

Object	z	FWHM(H β) ^a (km s ⁻¹)	log [λL_{λ} ^b /ergs s ⁻¹]	log [M/M_{\odot}] ^c (H β , L_{λ} , SE)
(1)	(2)	(3)	(4)	(5)
PG 1402+261	0.16400	1873.7	44.983 ^{+0.017} _{-0.018}	7.944 ^{+0.081} _{-0.100}
PG 1404+226	0.09800	787.3	44.379 ^{+0.017} _{-0.018}	6.889 ^{+0.080} _{-0.098}
PG 1415+451	0.11400	2591.2	44.561 ^{+0.017} _{-0.018}	8.014 ^{+0.080} _{-0.098}
PG 1416-129	0.12900	6098.0	45.135 ^{+0.037} _{-0.041}	9.045 ^{+0.083} _{-0.103}
PG 1425+267	0.36600	9404.7	45.761 ^{+0.100} _{-0.130}	9.734 ^{+0.097} _{-0.126}
PG 1427+480	0.22100	2515.3	44.759 ^{+0.021} _{-0.022}	8.088 ^{+0.081} _{-0.099}
PG 1435-067	0.12900	3156.9	44.918 ^{+0.036} _{-0.040}	8.365 ^{+0.082} _{-0.102}
PG 1440+356	0.07700	1393.5	44.546 ^{+0.014} _{-0.014}	7.468 ^{+0.080} _{-0.098}
PG 1444+407	0.26700	2456.5	45.203 ^{+0.023} _{-0.024}	8.289 ^{+0.083} _{-0.102}
PG 1448+273	0.06500	814.7	44.482 ^{+0.011} _{-0.011}	6.970 ^{+0.080} _{-0.098}
PG 1501+106	0.03600	5454.1	44.285 ^{+0.010} _{-0.011}	8.523 ^{+0.079} _{-0.097}
PG 1512+370	0.37100	6802.7	45.602 ^{+0.030} _{-0.032}	9.373 ^{+0.085} _{-0.106}
PG 1519+226	0.13700	2187.3	44.710 ^{+0.019} _{-0.020}	7.942 ^{+0.081} _{-0.099}
PG 1534+580	0.03000	5323.5	43.687 ^{+0.010} _{-0.011}	8.203 ^{+0.080} _{-0.097}
PG 1535+547	0.03800	1420.4	43.961 ^{+0.010} _{-0.011}	7.192 ^{+0.079} _{-0.097}
PG 1543+489	0.40000	1529.2	45.445 ^{+0.037} _{-0.041}	7.998 ^{+0.085} _{-0.105}
PG 1545+210	0.26600	7021.7	45.428 ^{+0.023} _{-0.024}	9.314 ^{+0.084} _{-0.104}
PG 1552+085	0.11900	1377.0	44.704 ^{+0.015} _{-0.015}	7.537 ^{+0.080} _{-0.099}
PG 1612+261	0.13100	2490.9	44.717 ^{+0.026} _{-0.028}	8.058 ^{+0.081} _{-0.100}
PG 1626+554	0.13300	4473.8	44.580 ^{+0.026} _{-0.028}	8.498 ^{+0.081} _{-0.099}
PG 1704+608	0.37100	6552.4	45.702 ^{+0.030} _{-0.032}	9.391 ^{+0.086} _{-0.107}
PG 2112+059	0.46600	3176.4	46.181 ^{+0.034} _{-0.037}	9.001 ^{+0.089} _{-0.112}
PG 2209+184	0.07000	6487.5	44.469 ^{+0.012} _{-0.013}	8.766 ^{+0.080} _{-0.098}
PG 2214+139	0.06700	4532.0	44.662 ^{+0.097} _{-0.126}	8.551 ^{+0.093} _{-0.118}
PG 2233+134	0.32500	1709.2	45.327 ^{+0.027} _{-0.028}	8.036 ^{+0.083} _{-0.103}
PG 2251+113	0.32300	4147.2	45.692 ^{+0.026} _{-0.028}	8.989 ^{+0.085} _{-0.106}
PG 2304+042	0.04200	6486.8	44.066 ^{+0.097} _{-0.126}	8.564 ^{+0.092} _{-0.117}
PG 2308+098	0.43200	7914.3	45.777 ^{+0.101} _{-0.131}	9.592 ^{+0.098} _{-0.126}

^aFWHM(H β) measured in the single-epoch spectrum in units of km s⁻¹. Values are adopted from Boroson & Green (1992) and are corrected for spectral resolution as described in the text.

^bThe luminosities at 5100Å were computed based on the spectrophotometry of Neugebauer et al. (1987) and Schmidt & Green (1983) as explained in Paper I.

^cThe central mass (and uncertainties) estimated based on single-epoch optical spectroscopy and the calibrated relationship of eq. (5).

Note. — Optical parameters and single-epoch estimates of the central black hole in the PG quasars studied by Boroson & Green (1992) without robust mass measurements based on reverberation mapping techniques.